Winter 1-1-2020

Effect of Geometry And Material on the Response of A Shape Memory Alloy (sma) Earthquake Damper

Anthony Addai Boateng
Cleveland State University

EFFECT OF GEOMETRY AND MATERIAL ON THE RESPONSE OF A SHAPE MEMORY ALLOY (SMA) EARTHQUAKE DAMPER

ANTHONY ADDAI BOATENG

Bachelor of Civil Engineering

Takoradi Technical University

July 2017

Submitted in partial fulfillment of requirements for the degree

MASTER OF SCIENCE IN CIVIL ENGINEERING

at the

CLEVELAND STATE UNIVERSITY

December 2020

DEDICATION

This work is dedicated to my family, academic advisor, professors, friends and course mates who have gave me all the support I needed through my entire school activities.

We hereby approve thesis

of

ANTHONY ADDAI BOATENG

Candidate for the Masters of Civil Engineering degree.

For the Department of

Civil and Environmental Engineering

And

CLEVELAND STATE UNIVERSITY'S

College of Graduate Studies by

_____

Dr. Josiah Owusu-Danquah
Advisor, Chair

_____

Department & Date

_____

Dr. Srinivas Allena

_____

Department & Date

_____

Dr. Lutful I. Khan

_____

Department & Date

December 30th, 2020

Student's Date of Defense

EFFECT OF GEOMETRY AND MATERIAL ON THE RESPONSE OF A SHAPE MEMORY ALLOY (SMA) EARTHQUAKE DAMPER

ANTHONY ADDAI BOATENG

ABSTRACT

Shape memory alloys (SMAs), such as Nitinol (i.e., NiTi), are of numerous importance in engineering applications due to their exceptional superelasticity and shape memory properties. Applications of a Shape Memory Alloy (SMA) in alleviating the seismic vibration response of civil infrastructure is attaining momentum. "Shape Memory" indicates that the material recollects its original formed shape. SMA has two simple properties, Super-Elasticity and Shape Memory Effect (SME). The "Super-Elastic" behavior revealed by SMA materials, allows a full recovery of strains up to 8% from big cyclic deformations, whereas developing a hysteretic loop. SME permits the material to recover the primary shape which is considered as re-centering mechanism. The mechanism of shape recovery comprises two crystallographic phases, Martensite and Austenite, and the transformations amongst them. The Austenite phase offers more stiffness than the Martensite phase. Phase transformation happens among Martensite and Austenite subject upon temperature and stress. These exceptional properties result in high damping and repeatable re-centering abilities which is an advantage in several civil infrastructure applications, exclusively in seismic vibration control devices.

In recent years, additive manufacturing (AM) processes have been used to produce complex NiTi components, which provide the ability to tailor microstructure and thus the critical properties of the alloys. SMAs have also been explored progressively by the earthquake engineering community, because of their extraordinary self-centering (SC) and energy-dissipating competences. This work analytically presents numerical investigations

executed to comprehend the numerical behavior of an SMA damper. Part of the numerical model is assessed against an experimental result by Zhai et al. (2020) and exhibited reasonable accuracy. The SMA damper with SC function under monotonic, fatigue cyclic and quasi-static cyclic loading is presented. The numerical results demonstrate that outstanding and stable flag-shaped hysteresis loops are exhibited in multiple loading cycles, indicating good energy dissipation, large deformation and ductility abilities. The stress-strain states with dissimilar phase transformation are also discussed in this work.

TABLE OF CONTENTS

LIST OF TABLES

Table Page

LIST OF FIGURES

Figure Page

CHAPTER I

INTRODUCTION

1.1 General

The damage of infrastructures due to strong ground wave permits new and inventive materials to be considered in designing earthquake resistant structures. Using shape memory alloys (SMAs), is one of the most prospective procedures for anti-seismic resistance of structures. SMA's owe their exceptional properties to solid-solid phase transformations that happen as an outcome of thermal or mechanical changes. SMA materials experience transformations between two stable phases, austenite and martensite, and get back to their original un-deformed point due to either an alteration of temperature, the shape memory effect; or elimination of stresses, the superelastic effect. The material behavior is hysteretic, however does not have some residual displacement. Due to this, a considerable quantity of energy dissipation capacity and re-centering abilities are accessible (Ozbulut, 2007).

Numerous researchers have explored the possible applications of SMA in civil infrastructures. Fugazza (2003) suggested a uniaxial constitutive model for Superelastic

SMA's for the installation into civil engineering structures. Auricchio (1995) established one and three dimensional thermo- mechanical constitutive models for SMA materials. Studies on the application of NiTi shape memory material able cause re-centering at the beam-column connection for steel frames was conducted by Penar (2005). Similarly, McCormick (2006) explored cyclical properties of large diameter shape memory alloys.

Notwithstanding the information that recent studies have added meaningfully to understanding of the possible usage of shape memory alloys in civil engineering applications, there are still several questions to be responded before life-sized applications can be instigated. To this end, this thesis implements a thermo-mechanical model wholly capable of simulating the super elasticity and shape memory effect. An outline has been suggested on how a structures can re-center itself after series of vibrations using an SMA damper.

1.2 Objective and scope of the study

The aim of this research is to numerically investigate the performance of an S-shaped earthquake damper using a superelastic SMA material. In this work, we use a commercial finite element code to simulate the earthquake damper under two material conditions, i.e., the elastic-plastic steel material and the superelastic NiTi SMA material. Presently, the only experimental data for comparison were those in literature for the SMA material point behavior. The experimental counterpart for the case of the SMA device simulation will form part of the future studies. Moreover, for computational purposes, we consider the effect of the type of the element used on the computational cost and accuracy of the results, i.e., beam element versus shell element versus solid element.

1.3 Organization of the thesis

The remainder of the thesis have been divided into four (4) chapters.

Chapter 2 presents literature review regarding properties of SMA materials.

Chapter 3 presents the finite element model and the SMA plate material. Also, a confirmation of the nonlinear finite element analysis is presented.

Chapter 4 implements a parametric design and presents results for several cases and discussion of the results.

Chapter 5 presents conclusions and future research recommendation.

CHAPTER II

LITERATURE REVIEW

2.1 General

Shape memory alloys (SMAs) or "memory alloyed metals" are special alloys in the class of memory materials/metals that can recover large amounts of deformation (up to a strain of 10%) under definite thermo-mechanical conditions. A vital feature of the SMAs is to undergo large superficially plastic strains and consequently recover these strains when load is removed, or heat is applied to the material. The most economical and well-known shape memory alloy is the nickel titanium alloys, known as nitinol (NiTi). NiTi had its properties revealed in 1962 as it was fabricated in order to make missile nose cone for the Naval Ordinance laboratory that could resist fatigue, heat and force of impact (Buehler et al. 1963), however, the first discovery of the shape was at 1932 (Ölander 1932). The distinctive property of shape memory is the basis for many applications of these materials, and several alloys are found to exhibit the shape memory effect. Well known low-cost and commercially available SMAs include the Fe-Mn-Si, Cu-Zn-Al, Cu-Al-Ni, Ni-Ti-Hf, Ni-Ti-Pd, Ni-Mn-Ga, alloys. For most practical applications, the NiTi-based SMAs are preferred due to their large recovery, outstanding corrosion resistance, biocompatibility,

superior ductility, stable transformation temperatures and easiness of electrical heating (Lagouda 2008, Duerig et al. 2013). Moreover, NiTi shows good resistance to wear and have superior energy absorption capacity. NiTi has been used for actuation, energy absorbing, and sensing. For actuators, NiTi offers numerous advantages, such as excellent power to mass ratio, maintainability, consistency, and clean and silent actuation. There are shortcomings such as low energy efficiency owing to conversion of heat to mechanical energy and difficulties in control due to hysteresis, nonlinearities, parameter uncertainties, and in the challenge of determining state variables such as temperature.

The major properties of SMAs are discussed below.

2.1.1 Phase transformation in SMAs

A phase transformation which occurs between these the austenite and martensite phases upon heating/cooling is the origin for the unique properties of the SMAs. The important properties of SMAs related with the phase transformation ae pseudoelasticity or superelasticity and shape memory effect. In SMAs, there are two crystal phases; stability in higher temperature gives rise to stronger austenite (A) phase and stability in a lower temperature, a weaker martensite (M) phase. The two phases contrast in their crystal structures. Austenite has a body-centered cubic crystal structure, while the martensite has a parallelogram structure, having up to 24 variations. When SMAs in martensite is subjected to external stress, they deform through a mechanism called detwining, which converts different martensite variants to a specific one variant that can accommodate the maximum elongation. Owing to its parallelogram structure, the martensite phase is weak and can be easily deformed. The austenite phase has only one possible orientation and shows relatively strong resistance to external stress (Duerig et al. 2013). The figure below

describes a stress-temperature-transformation plot and it is a schematic representation of the transformation regions for SMAs. The lines in the plot display the phase boundaries that discrete the two solid phases of an alloy. Typically, a stress-temperature-transformation plot shows the temperature along the x-coordinate and stress along the y-coordinate. The mechanism in which the crystalline structure of the austenite phase changes to martensite phase is lattice distortion and the transformation is martensitic transformation.

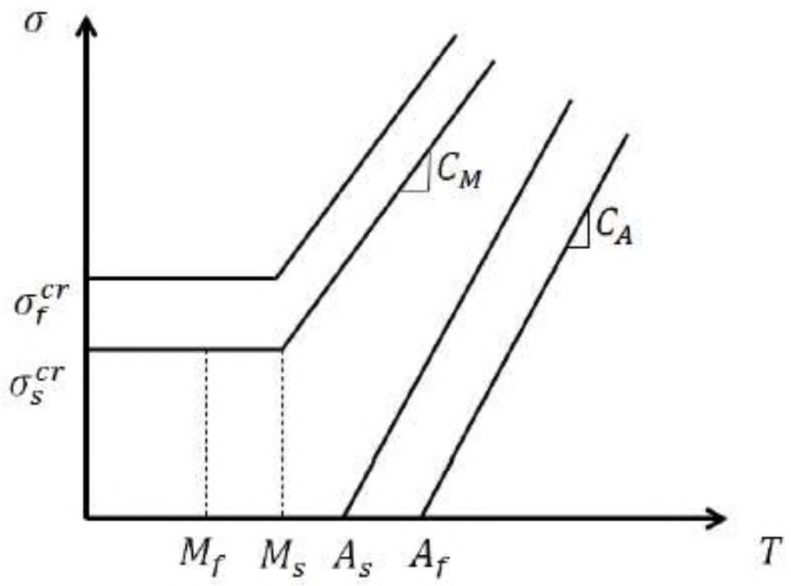

Figure 1: Shape memory material stress-temperature-transformation plot.

2.1.2 Damping properties

SMA used for damping can be both Martensitic and Austenitic. The damping is either from Martensite dissimilarities reorientation in the Martensitic material or from stress-induced Martensite in Austenitic material. Figure 2 a. below describes when subjecting an SMA sample to a series of deformation within its superelastic strain range, it dissipates a certain quantity of energy without permanent deformation. This outcome is

from the phase transformation, which is from Austenite to Martensite through loading and the opposite transformation during unloading, ensuring a net discharge of energy. Loading an SMA in the Martensite phase, produces a closely persistent stress after initial elastic deformation and shows strain hardening at larger strains. During unloading, there are some leftovers of residual strain at zero stress. Figure 2 a. also displays a generation of a full hysteresis loop round the origin in a Martensite composition of SMA. That is, a Martensite SMA dissipates a much higher quantity of energy as compared to Austenite SMA based on its larger hysteresis loop. Nonetheless, it has no re-centering ability like the Austenitic SMA. With the Martensite phase in tension–compression cycles, the maximum stress achieved in compression is found to be roughly twice that in tension (Figure 2 b), which is known as asymmetry in tension and compression behavior in SMAs. Though Superelastic SMA dissipates less energy than Martensitic SMA, its improvement is that, it is capable of dissipating a considerable amount of energy under repetitive load cycles with insignificant residual strain (Alam et al., 2007).

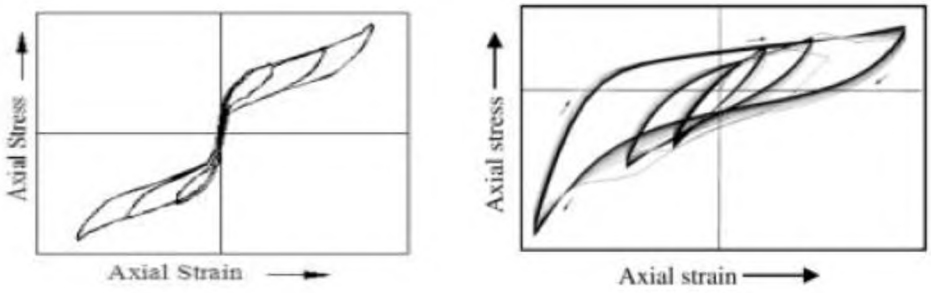

(a) (b)

Figure 2: Typical stress–strain curve of SMA under cyclic axial stresses: (a) Superelastic SMA; (b) Martensite SMA; (Alam et al., 2007).

2.1.3 Shape memory effect

The capability of an alloy to recover its pre-deformed shape upon heating is shape memory effect. This phenomenon occurs when the material is loaded such that the structure extends the detwinned martensite phase and then unloaded whereas the temperature is below the austenite start temperature (As). The strain accumulated is recovered at the transformation phase and the recovery is able to contain large forces (Funakubo 1987, Uchino 1998).

Shape memory effect are of two categories, specifically, one-way shape memory effect and two-way shape memory effect. When the alloy recalls only its high-temperature shape, it is one-way shape memory effect and when it recalls both the shapes at its high and low- temperatures, it is the two-way shape memory effect. Two-way shape memory effect is attained by "biasing" or "training" the SMA sample, by cycling several times between its low-temperature shape and high-temperature shape. The shape memory effect can be displayed vividly by the figure shown below.

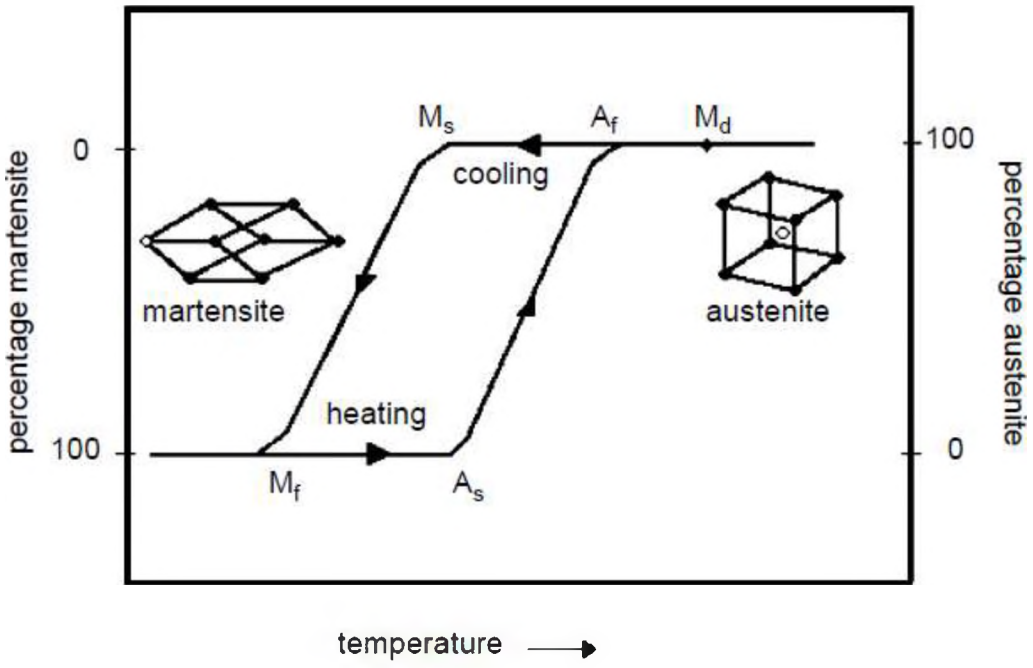

Figure 3: Transformation temperatures during shape memory effect

From figure 3, once SMA in its low-temperature martensitic form is heated, changes begin from the martensite to the austenite at austenitic start temperature, A_s. At austenitic finish temperature, A_f, it entirely transforms to austenite. A reverse change to martensite takes place at martensitic start temperature, M_s and at martensitic finish temperature, M_f, and all the austenite is wholly changed back to martensite upon cooling (Buehler and Wang 1968). The figure also describes a phenomenon in a combined stress-strain temperature diagram.

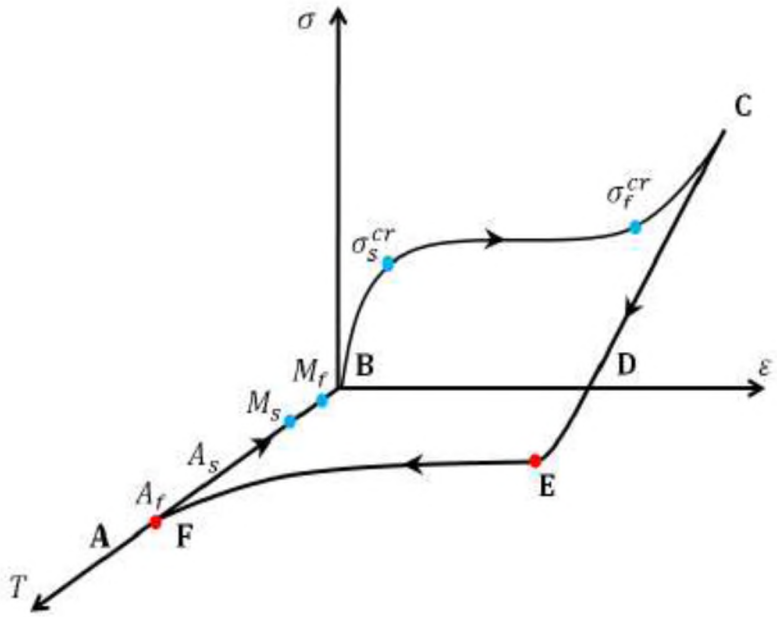

Figure 4: Shape memory effect path in stress-strain-temperature space

From a start point A, the material is originally in austenite phase. Cooling the material (alloy) down to a specific temperature, which is less than its martensite finish temperature (Mf) will result in the twinned martensite crystal at the point B. Loading the alloy at this point at the equivalent temperature, it alters to the detwinned martensite phase at the point C. Unloading the stress applied at this same temperature results in linear strain retrieval to point D. It remains the same in the detwinned martensite phase. Heating the alloy above the austenite start temperature (As) at point E, starts a transformation from the detwinned martensite phase to the austenite phase. This transformation improves the residual strain, fully recovered at point F, and at this point, the alloy passes the Austenite finish temperature. The stress-strain path is nonlinear based on the transformation phenomenon.

2.1.4 Superelasticity

Additional distinctive property of shape memory alloys is superelasticity or pseudo-elasticity. Contrasting the shape memory effect, superelastic behavior occurs deprived of any temperature modification, and this occurrence is witnessed in a slender range of temperatures above the Af (austenitic finish temperature). The capability of SMAs to recover huge amount of strains through mechanical loading and unloading is termed as the Pseudoelastic or superelastic.

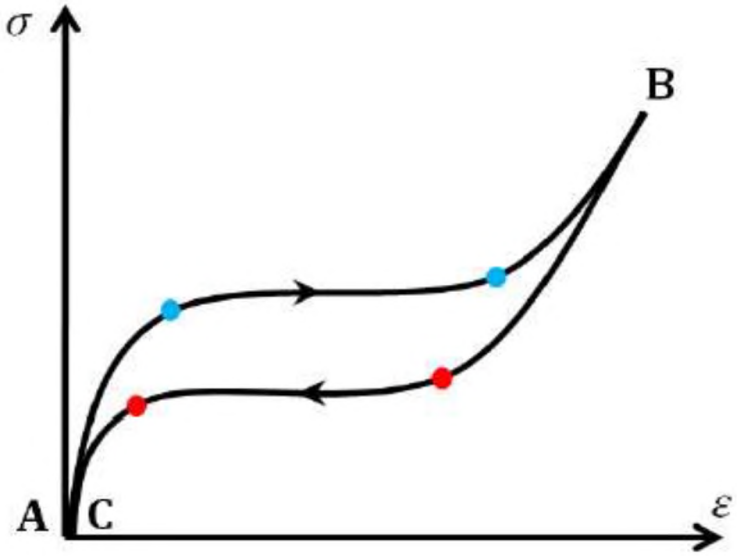

Figure 5: Superelastic stress-strain response of SMAs

Figure 5 demonstrations a representative superelastic stress-strain response of SMAs. The behavior which is thermo-mechanical, begins with a temperature above austenite finish temperature (A_f) where the material is completely in an austenite state at point A and further continue in loading by an applied force in making the detwinned martensite crystal form at point B. Throughout the alteration from austenite to the martensite state, the transformation strain is created. Upon unloading, the created strain is

completely recovered in the recessive transformation and the original form is achieved at point C. Stress-temperature-crystalline structure cycle of this kind of behavior is revealed on the transformation plot below.

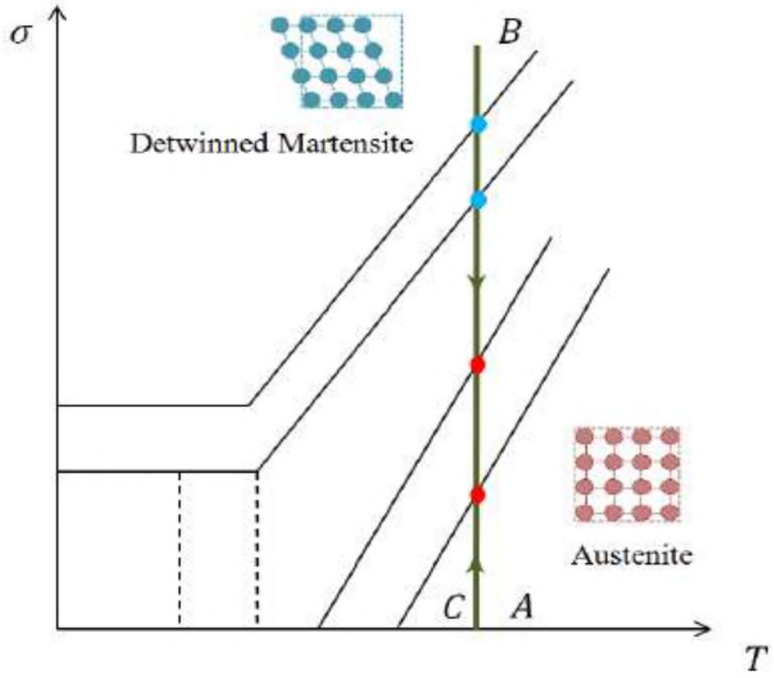

Figure 6: Superelasticity in phase diagram

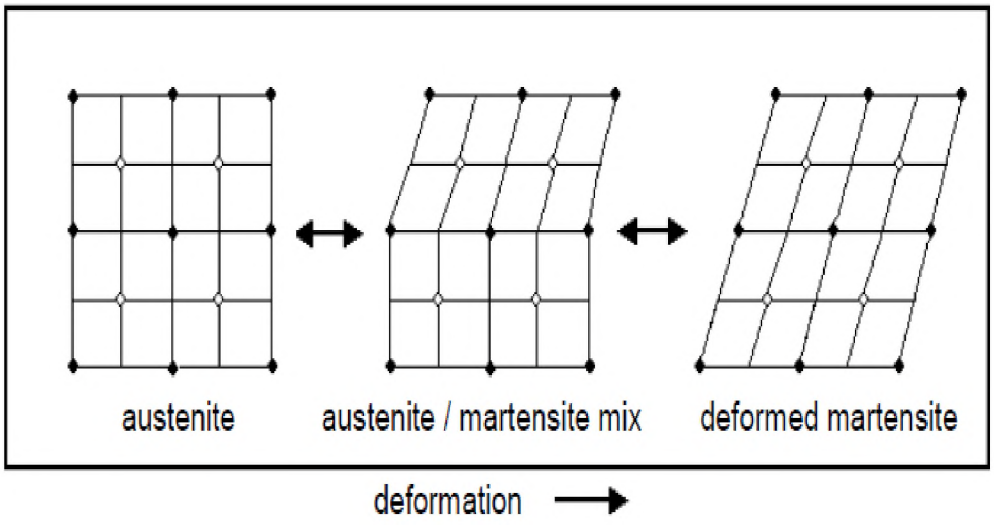

Figure 7: Lattice structure during superelastic deformation

2.1.5 Multi-axial loading behavior

When an SMA element is subjected to simple uniaxial tension or pure torsion loading and unloading situations, it offers a brilliant stress-strain hysteresis-like framework which is linked with the force/torque requirement of the device at a constant temperature. But there are also potential applications, in which the required force/torque profiles are more complex than simple hysteresis loops resulting from simple tension or torsion loading/unloading. In such instances, using the combination of tension-torsion loading paths might be a solution to attain a more adaptable reaction. Additional dynamic force in the engineering and processing methods of SMAs (Elahinia et al. 2012) is leading to the autonomy in assembly of complex SMA parts and structures with loading approaches other than modest tension or torsion. There is a substantial concentration in modeling the superlastic behavior of shape memory alloys, especially for NiTi materials. The experimental data which are used in developing and assessing the models are related to simple uniaxial tests in numerous instances. To develop consistent models, which are used to simulate general 3D structures subjected to complex loading conditions, it is of principal reputation to use multiaxial experiments. Sittner et al. (1995 and 1996) conducted out of phase non-proportional box and triangle tension-torsion experiments on Cu-based SMAs and validated the path reliance of the SMA mechanical response in the tension-torsion states. Related studies on Niti was piloted by (Rogueda et al. 1996) on pseudoelastic behaviour of a Cu Zn AI polycrystalline shape memory alloy under tension-torsion proportional and non-proportional loading tests. (Lim and McDowell 1999, McNaney et al.2003, Helm and Haupt 2002, and Grabe and Bruhns 2009) performed extensive proportional and non-proportional biaxial tests. Loading direction and loading sequence was revealed to affect the macroscopic behavior of SMAs.

Training an SMA refers to the procedure of repetitively loading and unloading the SMA material till its response becomes regular. The figure 8 describes a cyclic mechanical loading of a NiTi superelastic material. When trained the hysteretic response of the SMA material steadies and the inelastic strain steeps and dissolves.

In the training of an SMA material, at the close of the first cycle, some permanent plastic strain residues in the material. The supplementary permanent strain allied with each repeated cycle starts to progressively drop till it basically ends to further accrue. Training is a suggested method to be conducted on every NiTi component before practical application to avoid an unreliable strain response.

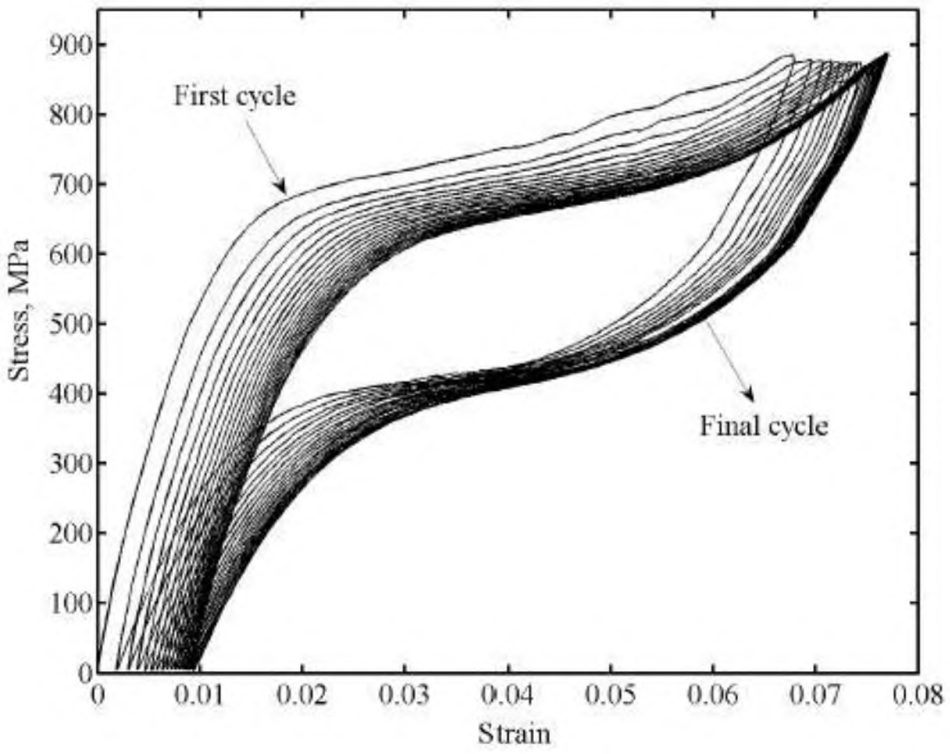

Figure 8: Training is required to be conducted on SMA to stabilize its cyclic response

2.1.6 Loading rate dependency

It has been proven that, increasing the strain rate in an SMA material causes a substantial temperature alteration in the material owed to the absorbed latent heat during the phase transformation (Grabe et al. 2009). The forward phase transformation (Austenite to the Martensite) is exothermal and the reverse transformation (Martensite to Austenite) is endothermal. Throughout the forward transformation, the temperature of the SMA surges making austenite more steady and at the reverse transformation, the temperature of the SMA declines making martensite more stable. This temperature development results in different stress plateaus in the dynamic loading conditions, resulting to different values of hysteresis loop area and energy dissipation.

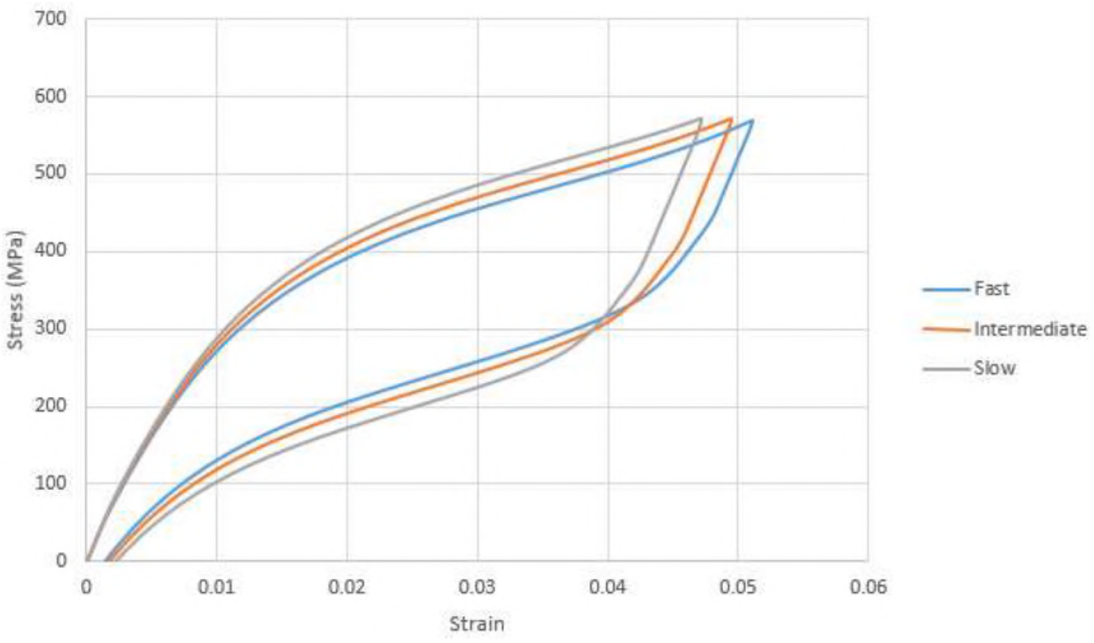

Figure 9: Development of the mechanical response at different loading rates

Figure 9 shows a typical NiTi under uniaxial loading with three loading rates agreeing to strain rates of 0.047/s, 0.049/s and 0.051/s for slow, intermediate and fast

respectively. The transformation finish stresses and the slopes of the phase transformation plateaus rise with increasing strain rate.

CHAPTER III

MATERIAL AND METHODS

In this chapter, the material properties, plate geometry, boundary conditions, the employed finite element model and mesh convergence study are discussed. Loading cases such as monotonic loading, fatigue cyclic loading and quasi-static cyclic are also deliberated.

3.1 Constitutive model

The performance of SMA's demonstrate a high level of strength, because it depends on stress and temperature, and it is steadily associated with the crystallographic phase of the material and the thermodynamics underlying the transformation procedures. For these efforts, simulation taking improvement of the uncharacteristic properties of the SMA has to be created on a right constitutive model.

3.1.1 Overview of constitutive modeling of shape memory alloys

Modeling of SMA behavior such as shape memory effect (SME) and pseudo-elasticity (PE) or superelasticity has been a lively area of research for the last two decades. The modeling strategies can be considered as phenomenological and thermo-dynamical strategies (Rashid, 2013).

Early phenomenological theories were revealed by Liang and Rogers (1990). One-dimensional model which does not precisely account for the twin effects of stress induced transformation and Martensite reorientation were presented. Barrett and Sullivan (1995) presented a model that have depiction of generalized one-dimensional constitutive the shape memory phenomena, using a mixture of phenomenological relations to outline the effects of multi-axial states of stress on the development of Martensite volume fraction. Nevertheless, it does not lead to a complete set of integrable constitutive equations that may be considered for numerical simulation.

Brinson and Lammering (1993) utilized the Brinson's (1993) model in 3D version to execute FEM simulation. Restrictions of this model defines the transformation-induced plasticity as a system of non-linear elastic behavior, and does not differentiate amid deformation caused by the transformation and reorientation events.

Thermodynamics-based models to investigate the shape memory alloys are also discussed in literature. However, thermodynamic models bound the options of material behavior as described by Boyd and Lagoudas (1996). Therefore, a suitably constructed phenomenological theories are effortlessly confirmed to have no substantially abhorrent characteristics and are regularly easier to comprehend and implement (Choudhry and Yoon, 2004).

Models centered more on classical plasticity methods have been reviewed by Berveiller et al. (1991); Auricchio and Talyor, (1996) and Lubliner and Auricchio, (1996). Lubliner and Auricchio (1996) model is comprehensive in such that, it accounts for the likelihood of visco-plastic deformation in Martensite and Austenite phase.

From the discussion so far, where there has been general attention paid to the constitutive modeling of shape memory alloys, there is no model that accounts for several phenomena of interest at the same time and yet simple enough to be practicably implemented (Saeedvafa, 2001).

Therefore, a computational model centered on phenomenological method is suggested for the effective and precise simulation of shape memory alloy and devices. For this thesis, we used the phenomenological model developed by Saleeb et al. (2010). The mathematical details and construct of the model can be found in literature Saleeb et al. (2011, 2013a, b and 2014). This SMA modeling structure is expressed as combination of multiple inelastic mechanisms to capture the hysteretic, nonlinear, and response of different normal and high temperature SMA materials under different thermomechanical loading. This model permits its application in geometrically complex SMA-based devices, subjected to variable degrees of displacements and rotations. In the current task, the focus was on the implementation of the model for structural analysis of the earthquake damper.

3.1.2 Materials

Two types of material models were used for the two different materials considered in this study. First, Saleeb et al. (2011) SMA model was used for SMA and the Deng et al. (2015) model was used for elastic-plastic material. For comparison and initial selection of the damper geometry, the experimental results from the work of Zhai et al. (2020) was used.

The targeted aims of applying the SMA model were: (1) to capture the experimentally observed cyclic superelastic behavior under tension and, (2) incorporate the calibrated/parameterized model as a user material subroutine, UMAT in ABAQUS

(Abaqus, 2013) to predict the response of the earthquake damper. The generality of the SMA model permits easy adaptation to different types of 3-D solid, shell and structural beam elements available in Abaqus FE code. In simulations, only static (i.e., no inertia forces considered) finite element analysis accounting for both material as well as geometric/kinematical nonlinearities were considered.

Table 1 shows the parameters for the SMA material model targeting the cyclic superelastic response of the NiTi material (Moghaddam et al. 2019) and the table 2 shows the parameters of the Deng et al. (2015) model for the elastic-plastic material properties (representing a steel material).

Table 1: Set of material parameters for the NiTi shape memory alloys

Parameters	**Unit**	**Value**
E	MPa	40,000
υ	-	0.3
n	-	5
μ	MPa.s	105
κ	MPa	40
$\beta_{(b)}$ for b =1,3,4,5	MPa	0.7,4,1,0.5
$\kappa_{(b)}$ for b =1,3,4,5	MPa	190,8,20,150
$H_{(b)}$ for b =1,3,4,5	MPa	50,000,100,25000,400

- E and υ are the SMA elastic modulus and Poisson's ratio respectively.
- κ, n, and μ are inelastic, rate dependent response governing parameters. Usually, κ denotes the critical transformation (''yield") stress at the lowest temperature of interest (below Mf).

- The ratio of $\kappa_{(b)}$ to $H_{(b)}$ defines the transformation strain series after which each hardening mechanism will reach its limiting values governed by $\kappa_{(b)}$.
- $\beta_{(b)}$ orders how fast each mechanism will show its maximum effect.

Table 2: Parameters for numerical material law (Deng et al. 2015)

σ0	**C1**	**Y1**	**C2**	**Y2**	**C3**	**Y3**	**C4**	**Y4**
185	22000	300	1600	120	6000	250	600	30

The C1, C2, C3 and C4 are the kinematic hardening parameters.

The stress-strain model relationship for the SMA and the elastic-plastic material for both experiment numerical analysis are presented in the figure below.

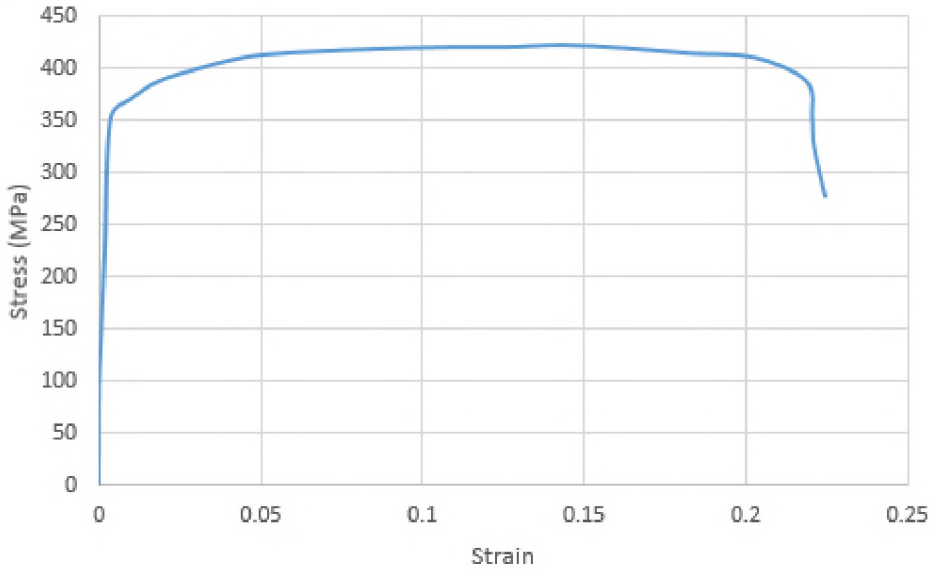

Figure 10: Stress–strain relationship of experimental results of elastic-plastic material

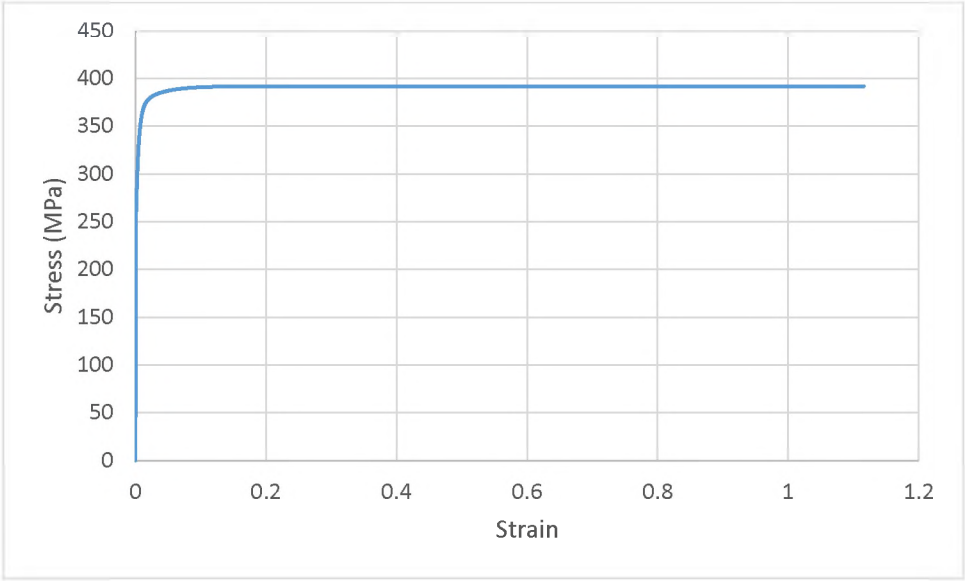

Figure 11: Stress–strain relationship of numerical analysis of elastic-plastic material

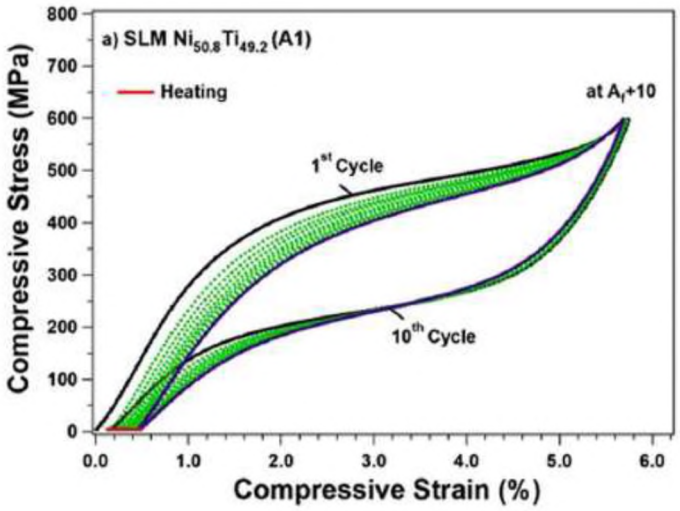

Figure 12: Addictive Manufactured (AM) NiTi experimental plot (Moghaddam et al, 2019)

In Figure 11, cyclic responses of a fabricated specimen are presented at austenite finish temperature (A_f) + 10 °C. This specimen was additively manufactured using selective laser melting (SLM) without a need for post-process heat treatment. The as-fabricated specimen established significant superelasticity behavior, i.e., strain recovery of

5.62% with recovery ratio of 98% in the first cycle, and the steadied strain recovery of 5.2% after 10 cycles.

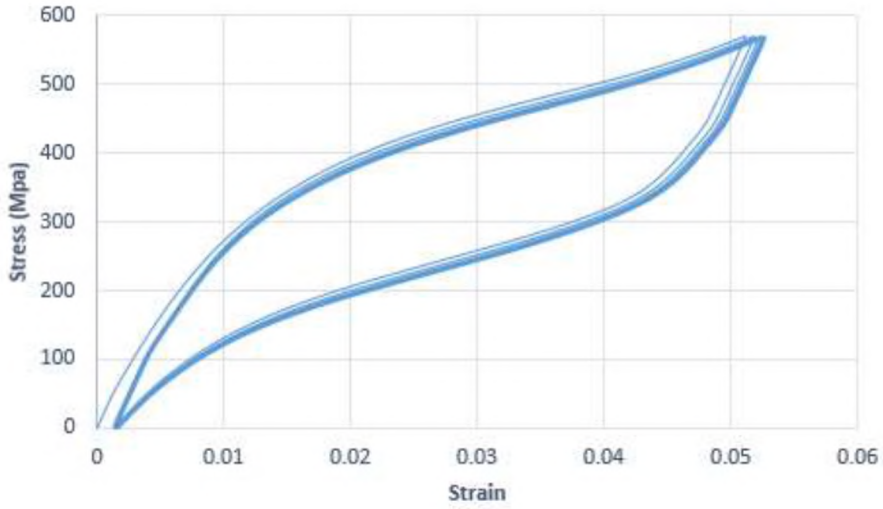

Figure 13: Stress–strain relationship of numerical analysis superelastic SMA coupon

The cyclic tensile tests of the coupon were piloted with a constant load of -300 N. The equivalent unloading process was conducted until the force returned to zero. The peak strain steadily increased with the number of cycles. The 5.1% strain cycle was followed by another monotonic load with an increased strain of 5.2%. Figure 12 shows a representative stress–strain relationship of the numerical analysis of superelastic SMA coupon. The highest strain was determined by the last cycle (5^{th} cycle) and was recorded as 5.4%. The onward phase transformation (from austenite to martensite) in the loading path started at approximately 510 MPa. However, a steady reduction in the strain recovery was observed with the increasing stress amplitude. For example, it increased to approximately 567 MPa after five cycles of constant applied load. The forward phase transformation plateau is comparable to the yield stress of steel material in seismic applications.

3.2 Finite element simulation

3.2.1 Geometry

The geometry of the S-shaped plate in its original undeformed condition is shown in the figure 13 below. For comparative purposes, the shape of the plate was chosen to be similar to that of Zhai et al. (2020) with the main difference being the material used. The S-shaped damper comprises of two plates to form a complete damper. Each part comprises of three parts; it contains a top end plate, bottom end plate and an S-shaped arc segment. This earthquake damper is wielding-free and suitable for fabrication, installation, inspection and post-earthquake replacement. It contains large deformation capacity and steady flexural-tensile yielding behavior, and the deformation behavior shifts slowly from flexure to tension with displacement increasing, which accordingly improves structural stiffness and strength at the high level seismic demands.

Commonly used metallic dampers can be classified into the axial yield type, shear-yield type, flexural-yield type as well as the shear flexural-yield type (Guo et al. 2020 and Chen et al. 2019). Typical axial-yield types are buckling restrained braces (Benavent 2010 and Mahrenholtz et al. 2015). Xu et al. (2016) suggested a new steel shear panel damper, made of low-yield-point steel plate, constrained flanges and stiffeners for the shear-yield type. Honeycomb structural fuse which absorbs energy by shear drift, and the design formulas of main parameters are given by test and finite element results was presented by Yang et al. (2020). Deng et al. (2015) studied the buckling restrained shear panel damper, and a shape optimization method centered on Von Mises yield criterion. In order to improve the performance of steel shear panels, Benavent (2010) developed a type of tube-in-tube damper with a chain of slits which makes the energy dissipation convert from shear

yielding to flexural-shear yielding. Dal et al. (2018) studied multiple slit dampers made-up by cutting steel plates to a set of simple beams and can turn the shear-type behavior into flexural type. Li et al. (2019) applied a chain of K-shaped plates to restrain out-of-plane buckling of the shear panel, which absorbs seismic energy through flexural deformation. The inventive shear-flexure combined damper can advance the energy dissipate performance and pinching effect of shear panels. Comparing shear yield damper, the flexural-yield damper has superior deformation and fatigue performance, such as the added damping and stiffness dampers (ADAS) (Whittaker et al. 1989), the triangular-plate added damping and stiffness (TADAS) dampers (Tsai 1993), bolted steel strip (Guo et al. 2020), U-shaped steel plate (Qu et al. 2019), annular steel plate damper (Chen et al. 2019), curved steel plate damper (Zheng et al. 2020), pure bending yielding dissipater (Zibasokhan et al. 2019) and hourglass-shaped strip damper (Lee et al. 2016). The seismic performance of metallic dampers with flexural-tensile behavior has been studied in recent years. Jarrah et al. (2019) presented precise flexural tensile type damper, dual-pipe damper (DPD) and piston metallic damper (PMD). The DPD is with a high deformation capacity of almost 36% of the pipe's outside diameter. Cyclic loading test was used to evaluate the low-cycle fatigue performance of the PMD. Nonetheless, the maximum loading displacement of roughly 5.8% of the pipe's inner diameter was comparatively small. The flexural-tensile type metallic damper shows unlimited improvement owing to its progressively increased secondary stiffness and strength as an outcome of tensile strengthening effect. As the axial tensile-compressive action occur in large displacement, the pinching effect and strength degradation can be outstanding, and the fatigue performance requires further study. The

fabrication and installation of all these flexural-tensile dampers require welding, which lead to application restrictions.

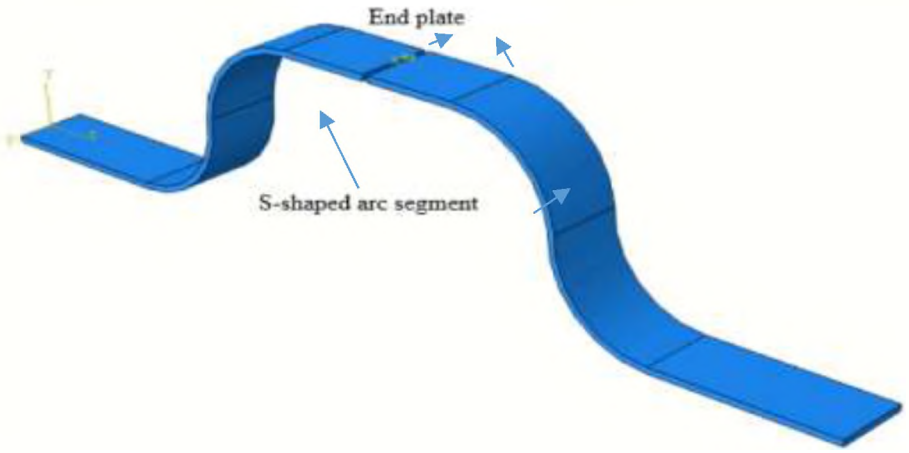

Figure 14: Schematic plot of original undeformed condition of S-shaped plate

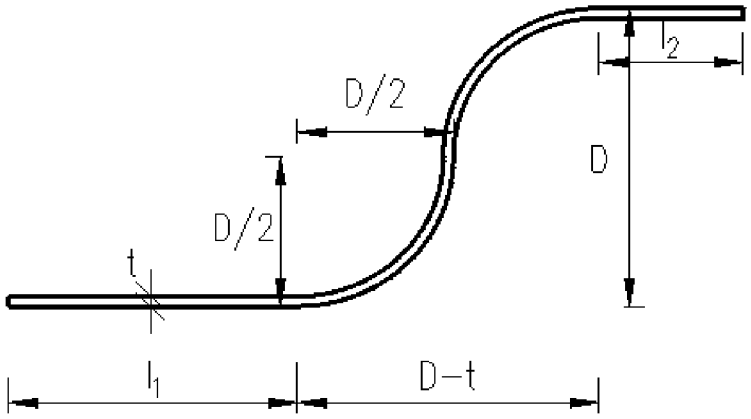

Figure 15: Geometric configuration of S-shaped plate

3.2.2 FE model

Finite element analysis (FEA) is performed using ABAQUS program (ABAQUS, v. 6.14 2017) to investigate the performance of the s-shape plate. The plate is modelled using three different types of element cases, i.e., a beam/wire element (B21), a shell element (S4) and a 3D solid element (C3D8) as shown in Figure 15. Details of the effect

of the type of the element used for the analysis is discussed in the next chapter. In the simulations, all the degree of freedom (DOFs) on the end surface of the bottom plate were restrained. All DOFs for the end plate of the top were coupled to a reference point and with an applied load in the X direction, i.e., degree of freedom one (U1).

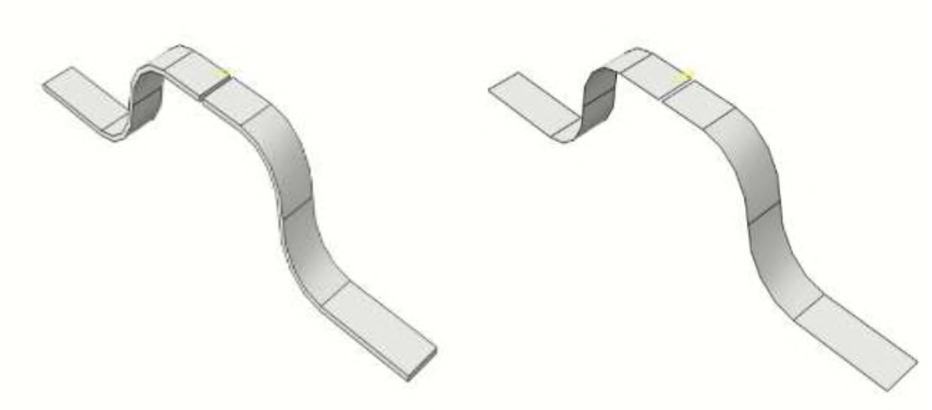

(a) 3D element (C3D8)

(b) Shell element (S4)

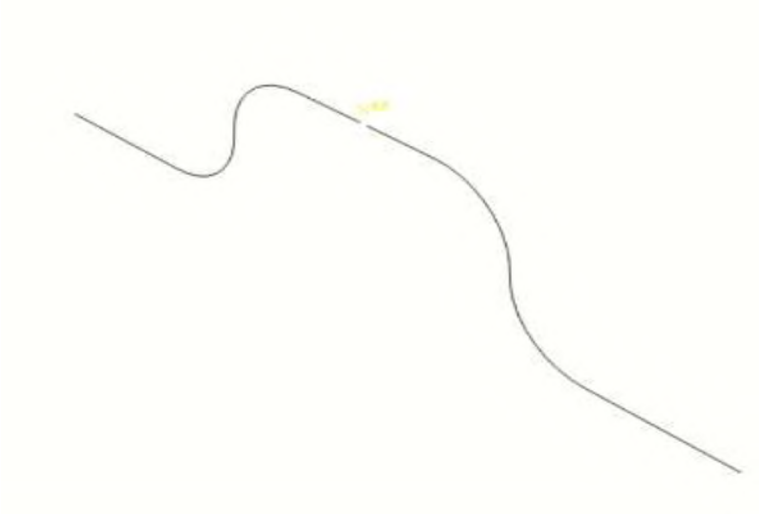

(c) Wire/beam element (B21)

Figure 16: Abaqus element cases

Table 3: Geometric dimensions of specimen (unit; mm)

Specimens	**D**	**b**	**t**	**l_1**	**l_2**
S1	108	40	3.59	100	50
S2	130	40	5.0	100	50
S3	150	40	6.0	100	50

3.3 Thermomechanical Loading Steps

A nonlinear static analysis using the unconditionally stable, fully implicit, backward Euler difference integration scheme (which have brilliant convergence and accuracy features) is used in the FE simulations.

Displacements are employed in all the three cases of monotonic loading, cyclic loading under increasing magnitudes, and fatigue test to the same displacement magnitude. The time-displacement amplitudes for all the three cases are shown the Figures below. A monotonic loading was adopted to determine the effect of the type of abaqus element and mesh size used in the simulation.

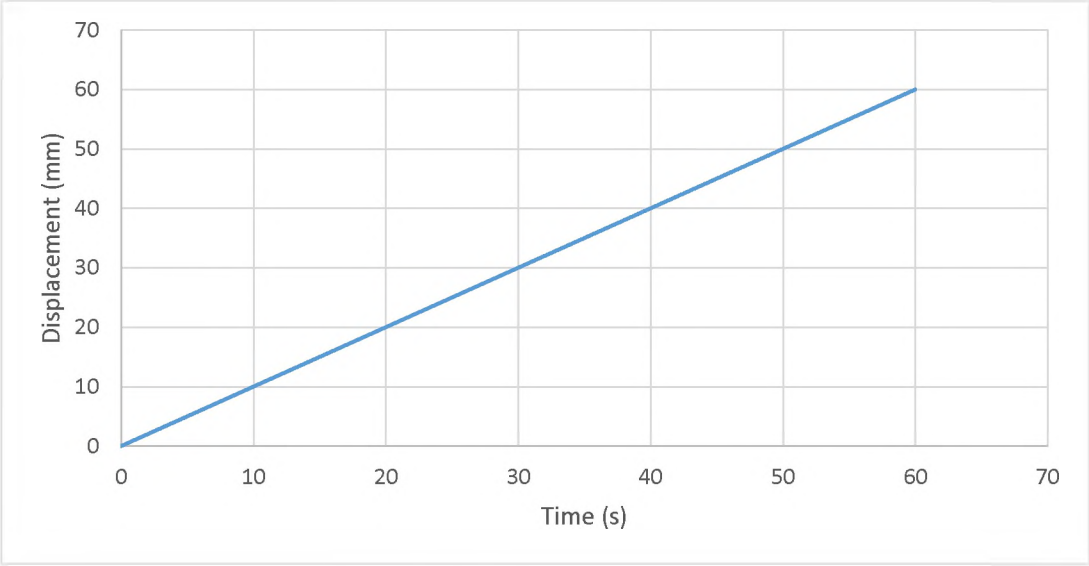

Figure 17: Monotonic loading protocol for specimens

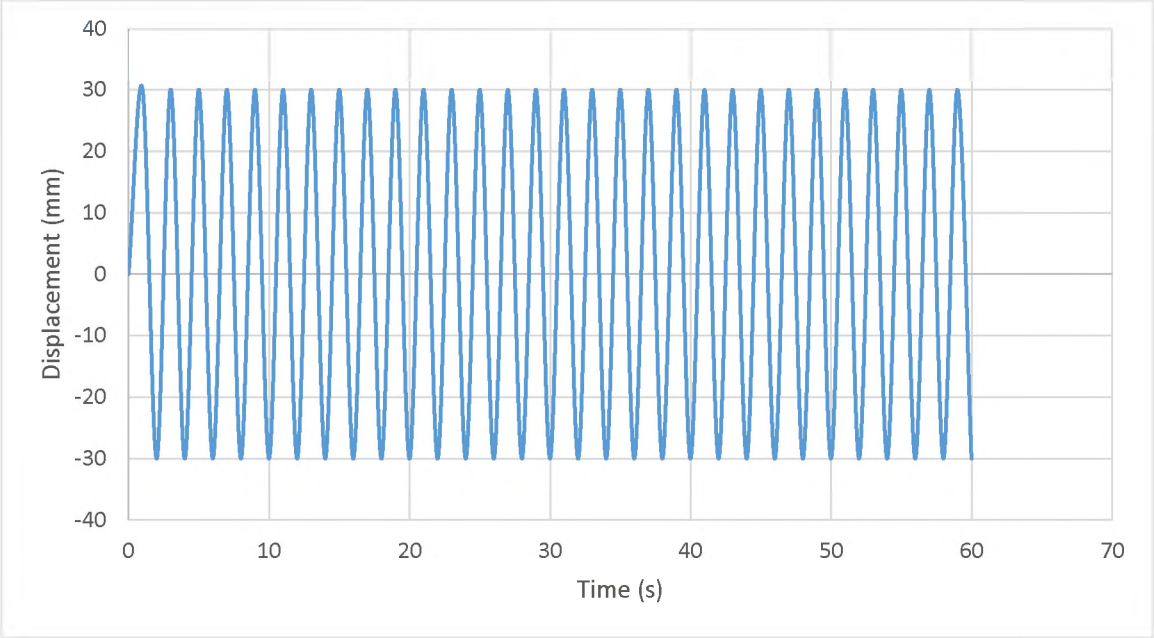

Figure 18: Fatigue cyclic loading protocol for specimens

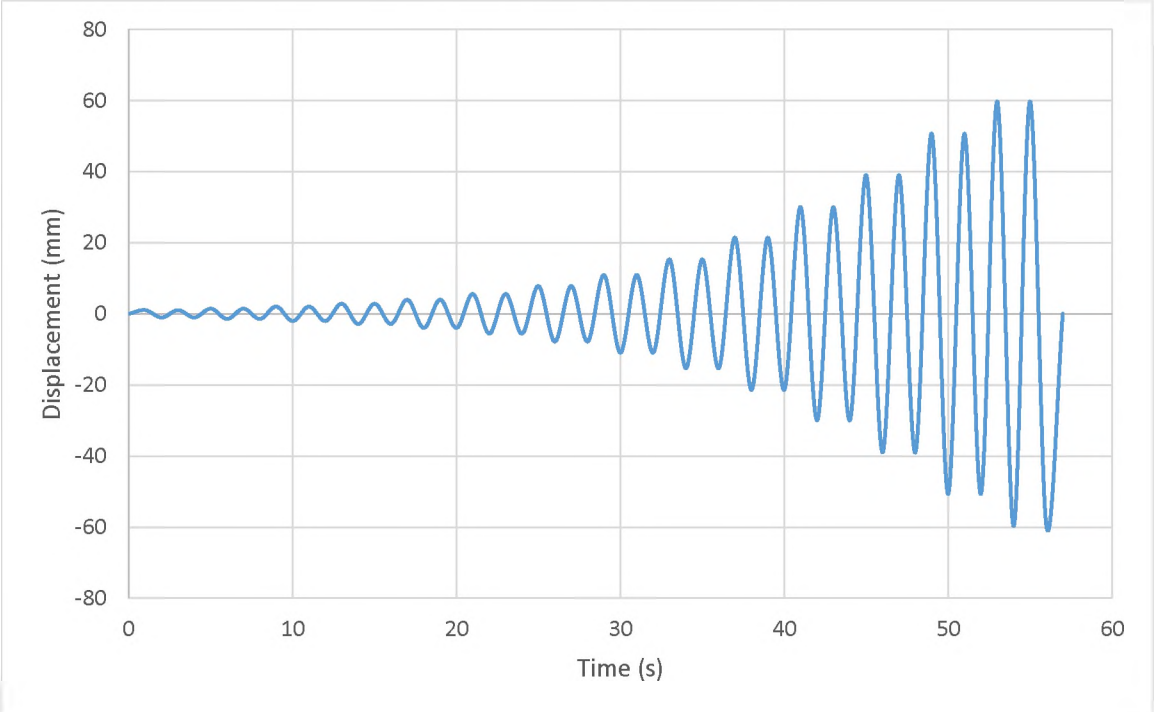

Figure 19: Quasi-static cyclic loading protocol for specimens

3.4 Mesh size

3.4.1 Mesh convergence study

The mesh convergence plots below characterize the response of the model, using mesh size and a displacement variable. During the process to show mesh convergence, different mesh sizes with the same applied displacement magnitude and boundary conditions are tested in the model. The response variables (for comparison) were the reaction force, RF1, in the X-direction, the maximum effective Von Misses stress and the Tresca criteria at the end of the applied displacement. The Von Mises criterion represents a critical value of the distortional energy deposited in the isotropic material whereas the Tresca criterion represents a critical value of the maximum shear stress in the isotropic material. Factually, the Tresca form is considered to be the more fundamental of the two, but the Mises form is seen as an engaging and mathematically convenient, therefore both the Von misses and the Tresca values were presented.

In this case, three (3) same S-shaped plates of an elastic material were considered for this study which is shown in the figure 19 below. Finer mesh was created by increasing the number of elements. Mesh sizes of 4, 5 and 6 were employed, which gave total number of elements to be 1790, 1088 and 728 respectively, which is expressed as 2.5:1.5:1. The mesh size 4 is considered as a finer mesh, mesh 5 as a fine mesh and mesh 6 as normal mesh. The results of the study are summarized in the table below.

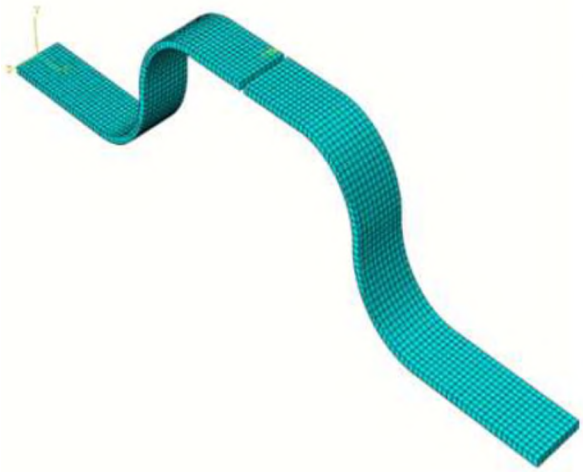

(a) Very fine mesh (1790 elements)

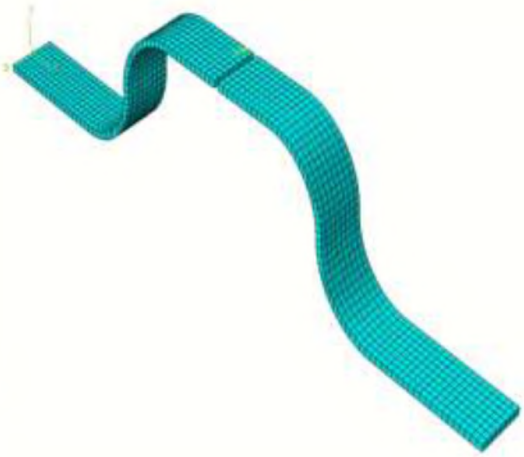

(b) Fine mesh (1088 elements)

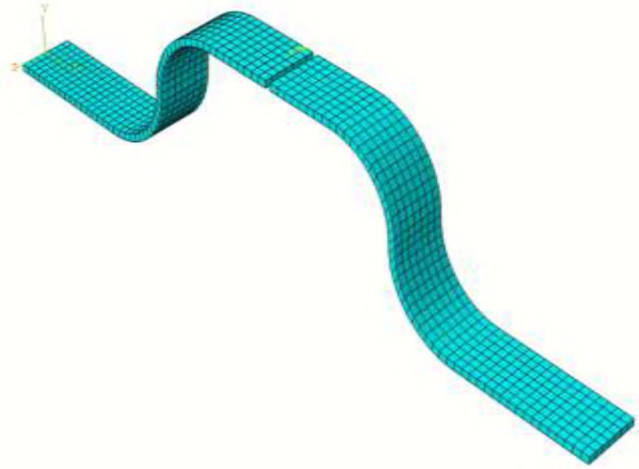

(c) Normal mesh (728 elements)

Figure 20: Meshed model

Table 4: Results of mesh convergence study

Mesh size	Elements	Time (s)	Reaction force, RF (kN)	Von Misses (MPa)	Tresca (MPa)
4	1790	1719	3.148	143	154
5	1088	1564	3.275	135	143
6	728	1056	2.493	49	55

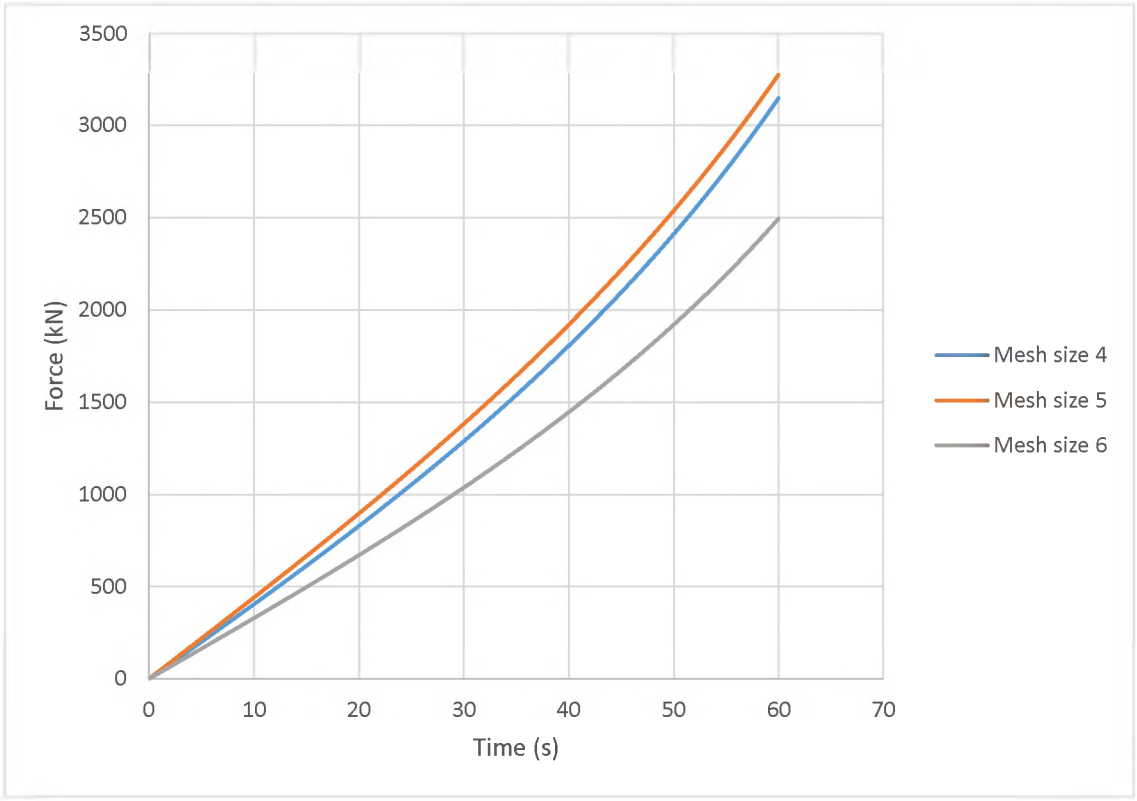

Figure 21: Force-time relationship for mesh sizes

The mesh refinement was studied to determine the suitable element size with reasonable computational time. To enhance computational efficiency, relatively fine mesh (with 1088 mesh) was used in the simulation for the 3D element types. This number of elements in the 3D solid elements will lead to a reasonable results and will be, adequate for qualitative representation of the complex stress distribution in the damper during the

cyclic loading process. The same process of convergence was used for the cases of the shell element and the beam element (although the comparisons are not shown here).

CHAPTER IV

NUMERICAL RESULTS AND DISCUSSION

4.1 Effect of the type of abaqus model element

Comparisons were made using the monotonic loading protocol to determine the effect of the type of abaqus model element used for the numerical test. Assessments were based on the execution time taken by each of the model elements and the value of the reaction force. A 60 mm displacement was applied to each of the model element to determine the force-displacement backbone curves and the execution time. A 3-dimensional 8 node solid (C3D8), a 4-node shell (S4) and a shear flexible beam, model elements were considered for this test.

The correlation between the numerical results of these model elements were not affected by the element, but total computational time was altered considerably.

The execution time for the C3D8 reached several seconds, which is 2428 seconds. The shell model element used a time of 195 second for the same applied displacement as the 3D. The beam/wire model element completed the 60 mm displacement at a lesser time as compared to the 3D solid and shell model element at a time of 95 seconds.

The model element results are presented below.

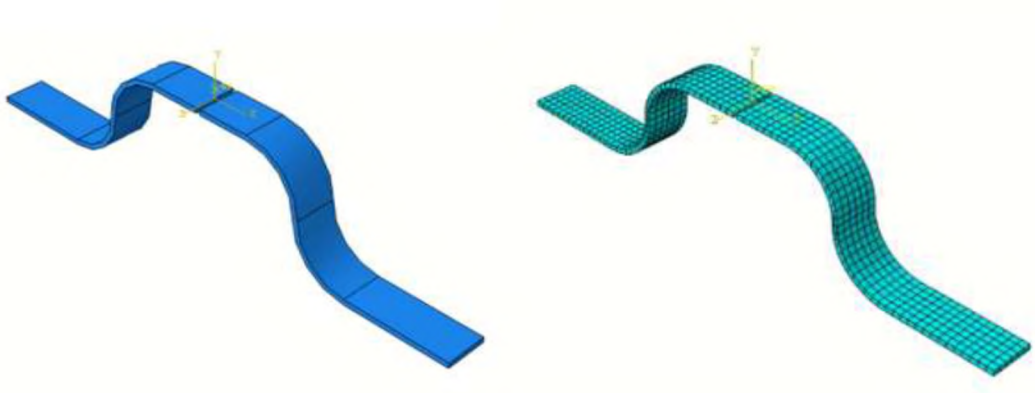

(a) Solid element model (b) Model meshing

Figure 22: (a) and (b) Established 3D finite element model of the plate

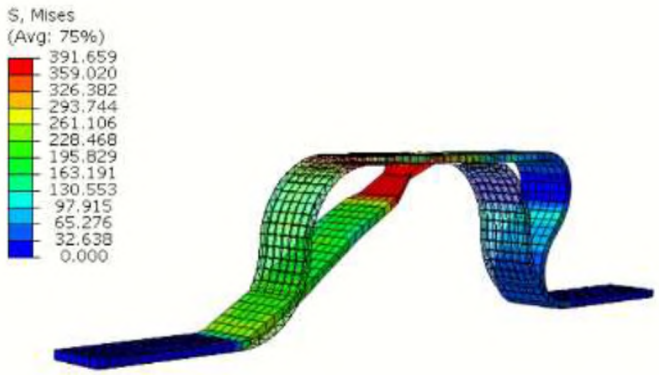

Figure 23: Von Misses stress of deformed 3D solid element, $\Delta = 60$ mm

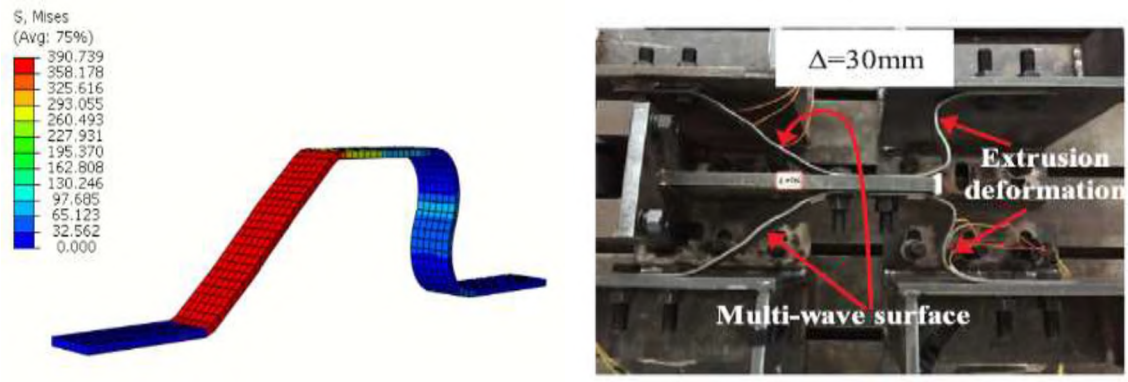

(a) FE model, Δ = 30 mm (b) Deformation from experiment (Zhai et al. 2020)

Figure 24: Comparison between the experiment and the simulation

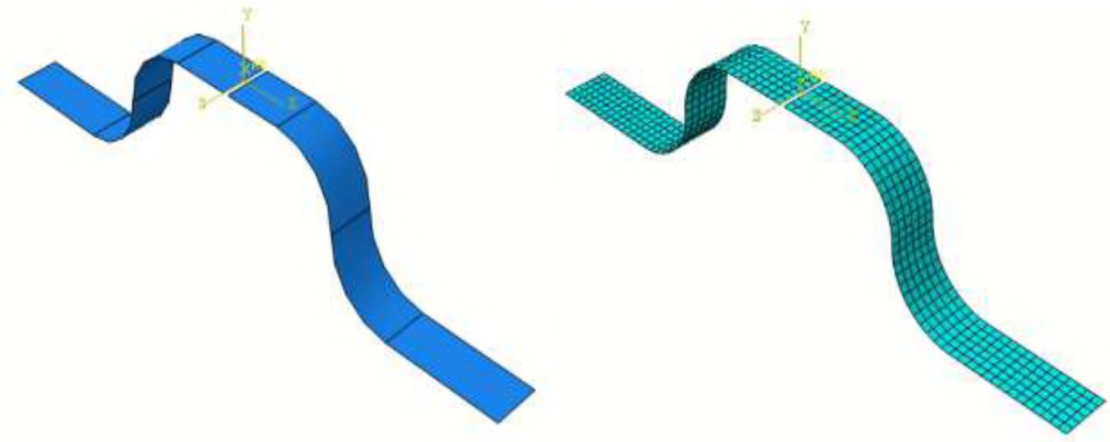

(a) Solid element model (b) Model meshing

Figure 25: Established 3D finite element model of the plate

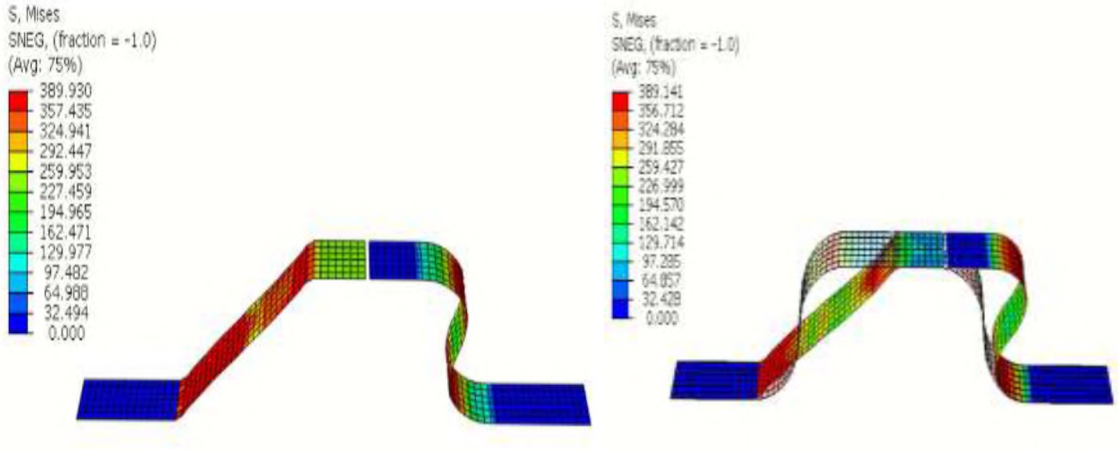

(a) $\Delta = 30$ mm (b) $\Delta = 60$ mm

Figure 26: (a) and (b) Von Misses stress of deformed shell element

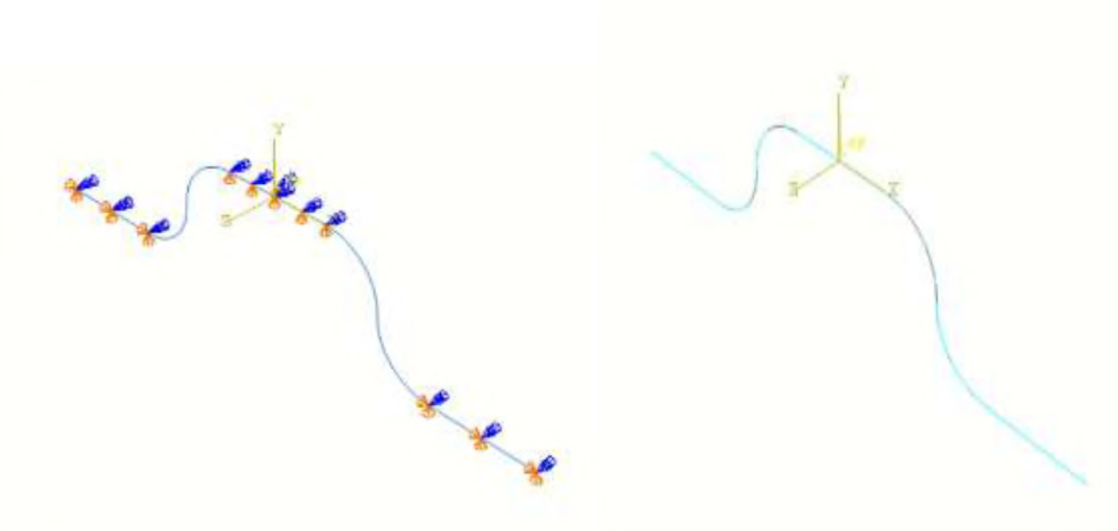

(a) Solid element model (b) Model meshing

Figure 27: (a) and (b) Established beam/wire finite element model of the plate

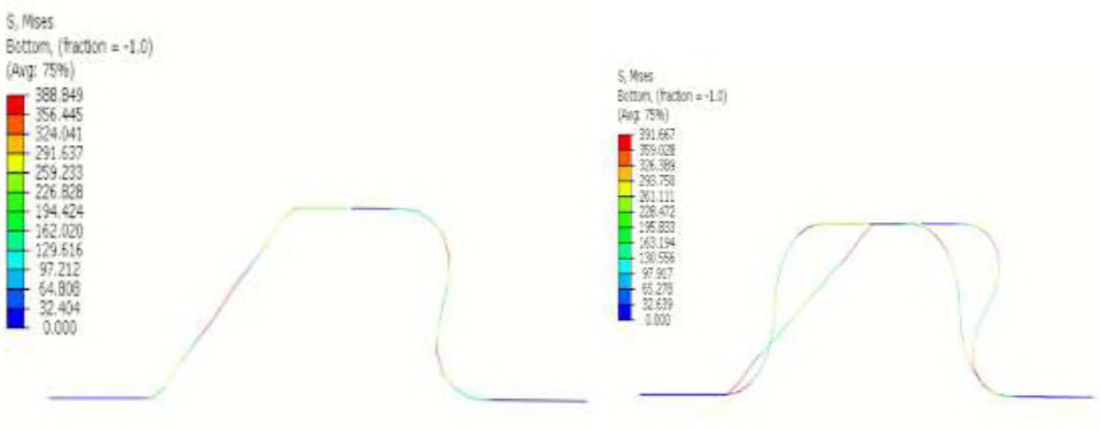

(a) $\Delta = 30$ mm (b) $\Delta = 60$ mm

Figure 28: (a) and (b) Von Misses stress of deformed beam/wire element

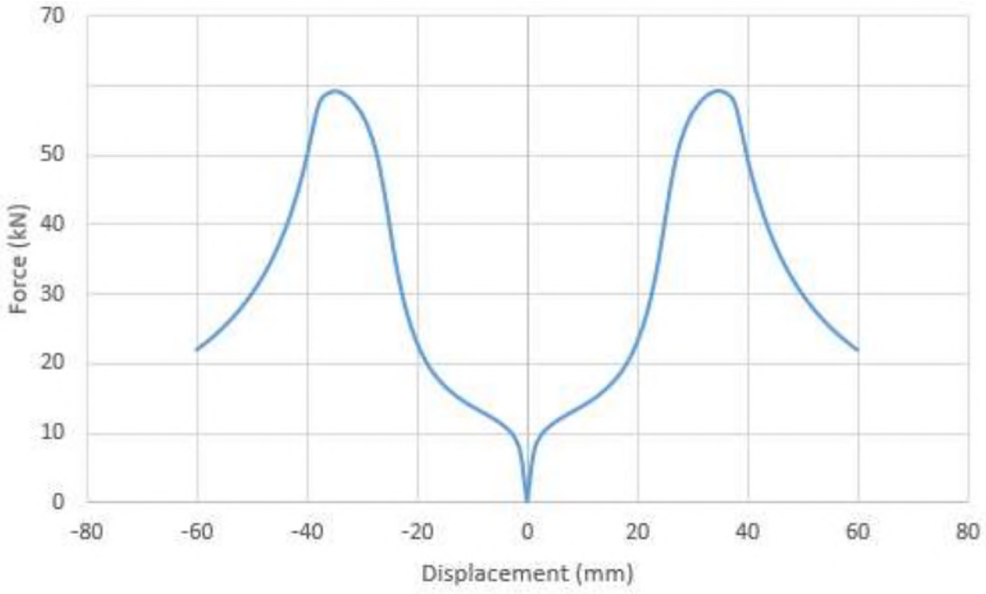

Figure 29: Force-displacement backbone curve for 3D FE model

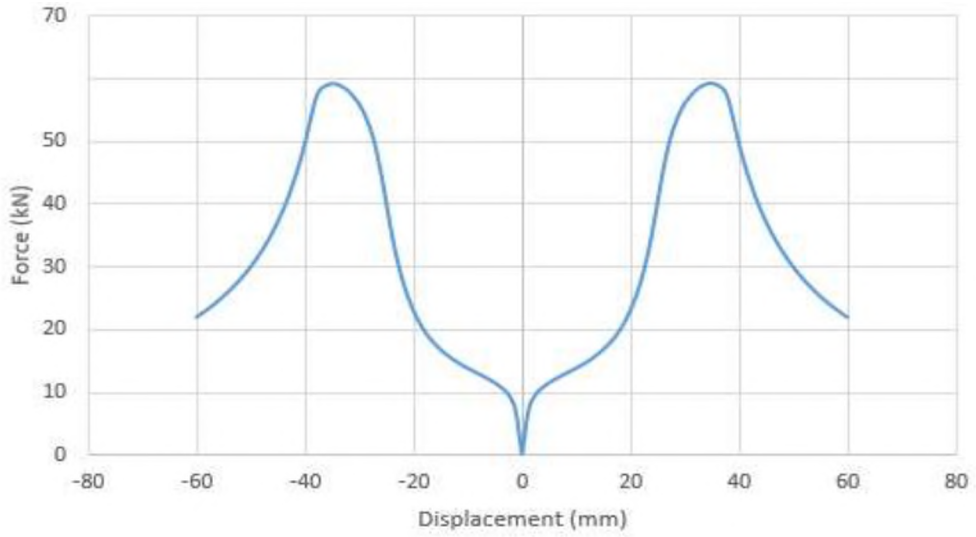

Figure 30: Force-displacement backbone curve for shell FE model

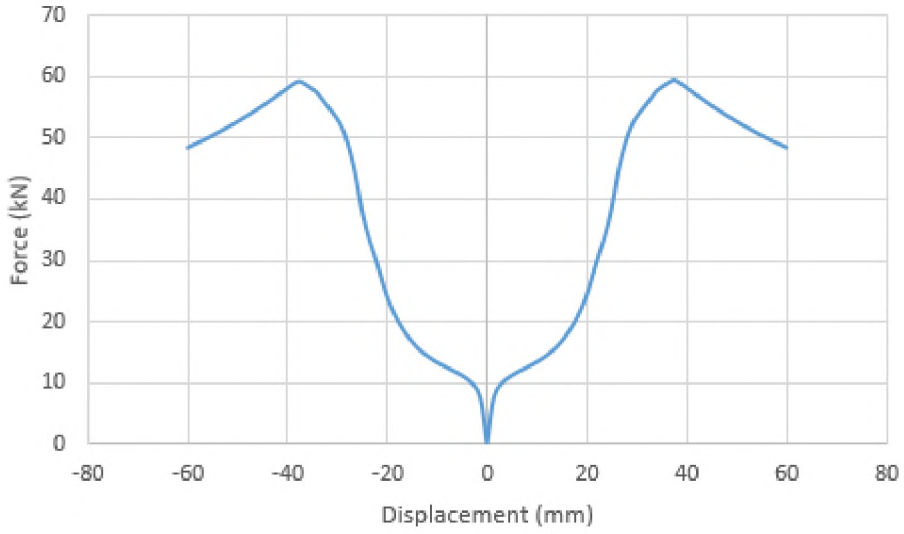

Figure 31: Force-displacement backbone curve for beam FE model

From the results presented, the reaction force for the 3D solid, shell and beam are 58 kN, 59 kN and 60 kN respectively. It can be understood from the force-displacement backbone curves of the model elements that the positive and negative (values of the applied displacements) make the response curves symmetrical. The backbone curve is in four phases: elastic phase, flexural yielding phase, tensile strengthening phase and fracture

failure phase. A multi-linear force-displacement model is established by Zhai et al. (2020) to characterize the backbone curve, and fundamental parameters are specified in a figure below, containing the initial stiffness k_e, the yielding displacement Δ_y and force F_y, the first yielding stiffness k_1, the second yielding displacement Δ_t and force F_t, the second yielding stiffness k_2, the peak force F_p and displacement Δ_p at tensile strengthening phase, the ultimate force Fu and displacement Δ_u. The yielding point (Δ_y, F_y) is the intersection of tangent lines of elastic and flexural yielding segments. The peak point (Δ_p, F_p) and Δ_u is gotten from the backbone curve. The second yielding point (Δ_t, F_t) is by two principles: (i) a point on tangent lines of flexural yielding segment; (ii) the area under multi-linear model before entering failure stage equivalents to the complement of backbone curve. Also, F_u is determined centered on the principle of energy balance. The stiffness k_1 and k_2 can be calculated from the equations below. Owing to the tensile behavior, the secondary stiffness k_2 is much higher than k_1.

$$k_1 = 0.001 k_e \left(\frac{D}{t}\right)^{2.88} \quad (1)$$

$$k_2 = 10^{-5} X\ 5.97 k_e \left(\frac{D}{t}\right)^{2.88} \quad (2)$$

$$k_e = 2.39 Eb \left(\frac{D}{t-1}\right)^{-2.63} \quad (3)$$

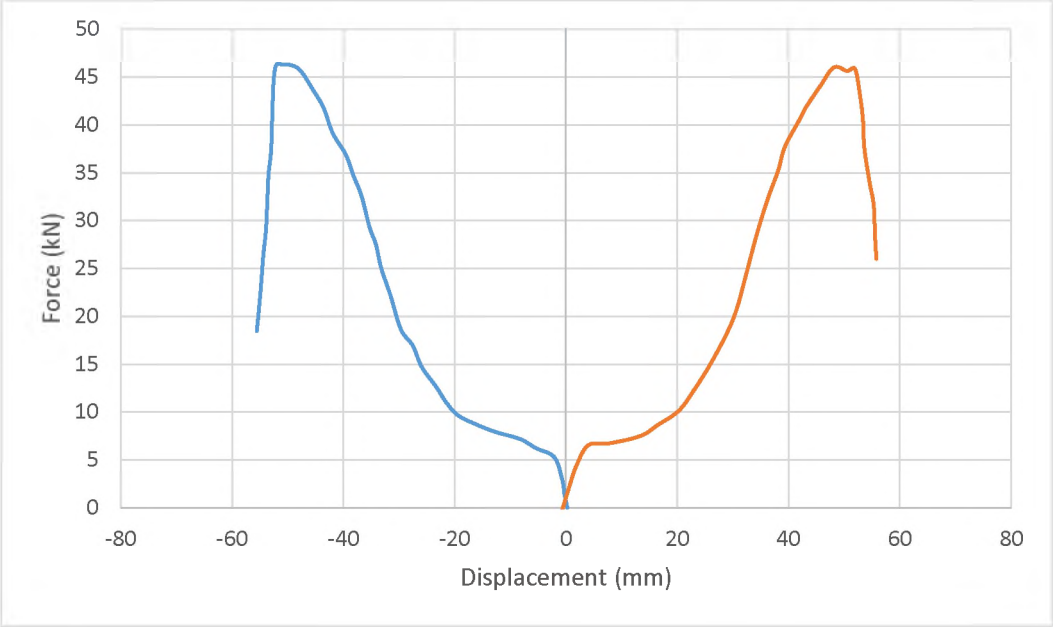

Figure 32: Force-displacement backbone curves of the plate from the experiment

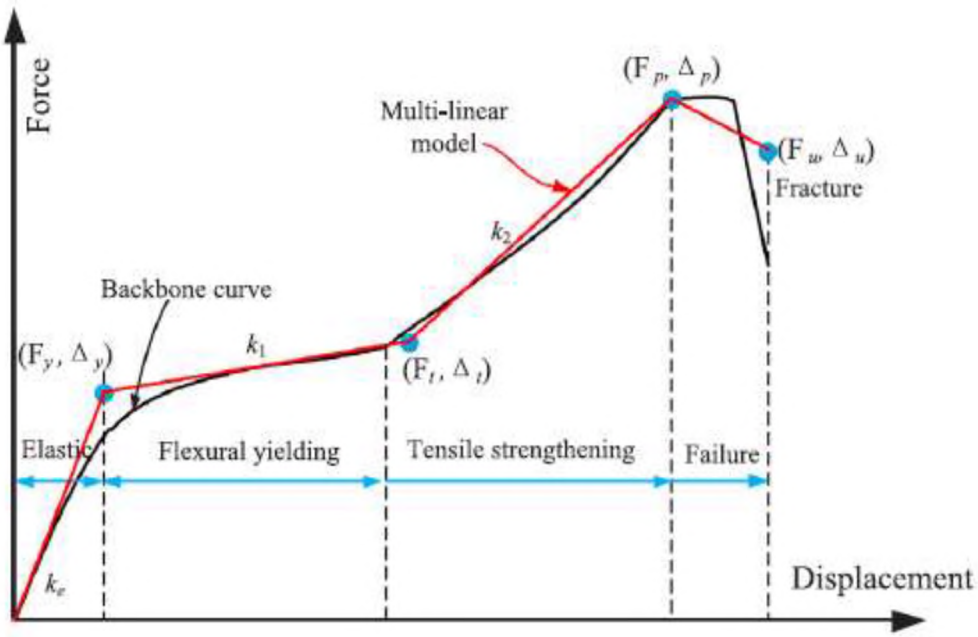

Figure 33: Idealize multilinear model for backbone curves (Zhai et al. 2020)

4.2 Effect of loading amplitude on fatigue performance

Fatigue is the failure of a structure element under the effect of cyclic stress. The failure occurs in three stages: crack initiation, crack propagation, and catastrophic overload

failure. The period of each of these three stages depends on several factors comprising magnitude and orientation of applied stresses, important raw material characteristics, processing history, etc. (Dagg and Lewis, 2009). Fatigue failures frequently result from applied stress stages expressively below those necessary to cause static failure.

In this test, the fatigue performances under different displacements were studied to compare the performance of the SMA to the elastic-plastic material. FE model with the same dimension of figure 26 (a) specimen was built, and displacement amplitude of 20 mm and 30 mm were applied with 30 cycles. Figure 3.13 and 3.14 show the force–displacement relationship curves the elastic-plastic and SMA material respectively. Under loading amplitude of 20 mm (0.185D) and 30 mm (0.278D), it is observed that as the displacement increases, the reaction force also increases, thereby producing an observed maximum force at the end of the 30 cycles for the 20 mm and 30 mm displacements were 24 kN and 53 kN respectively for the elastic-plastic material. The SMA material observed a maximum force of 27 kN and 89 kN for 20 mm and 30 mm displacements respectively. Hence, it can be established that the S-shaped plate has a large displacement capacity, nonetheless its fatigue performance under large displacement is inadequate due to the stress concentration and strength degradation. Fatigue performance of flexural-tensile type damper is delicate to displacement amplitude.

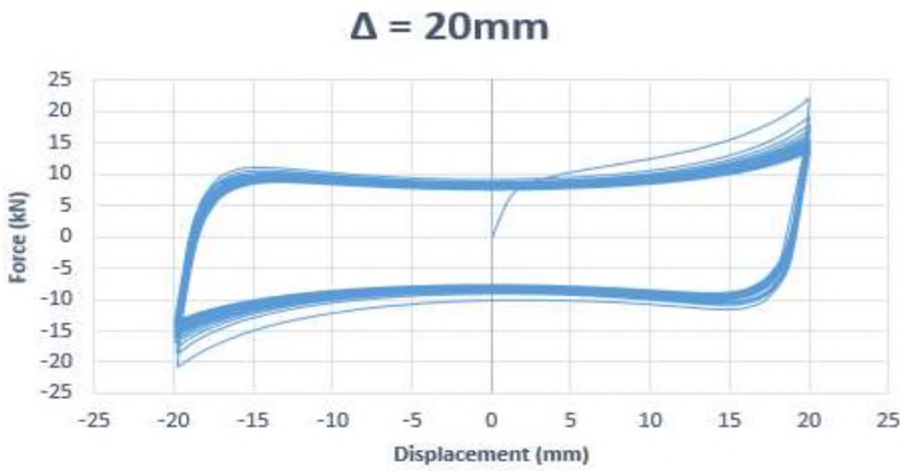

Figure 34: Force-displacement relationship of FE model subjected to fatigue cyclic loading (Elastic-plastic material) at a displacement of 20 mm

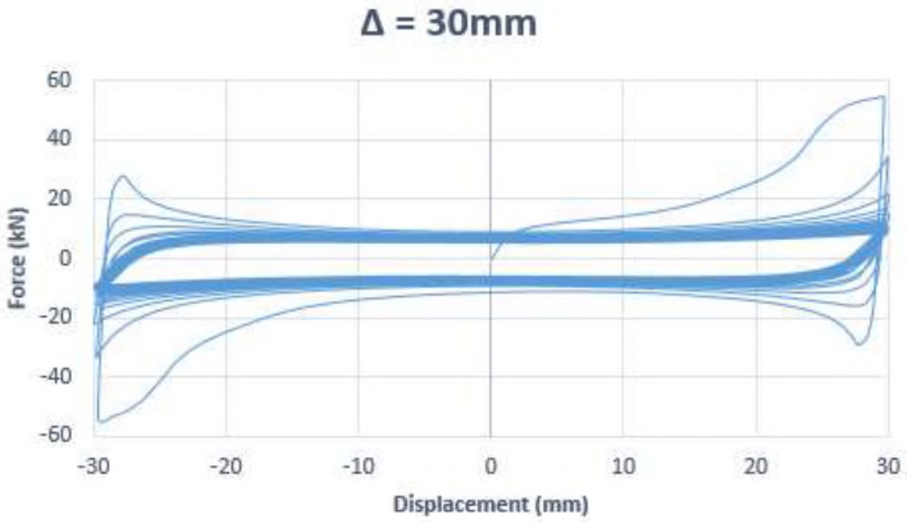

Figure 35: Force-displacement relationship of FE model subjected to fatigue cyclic loading (Elastic-plastic material) at a displacement of 30 mm

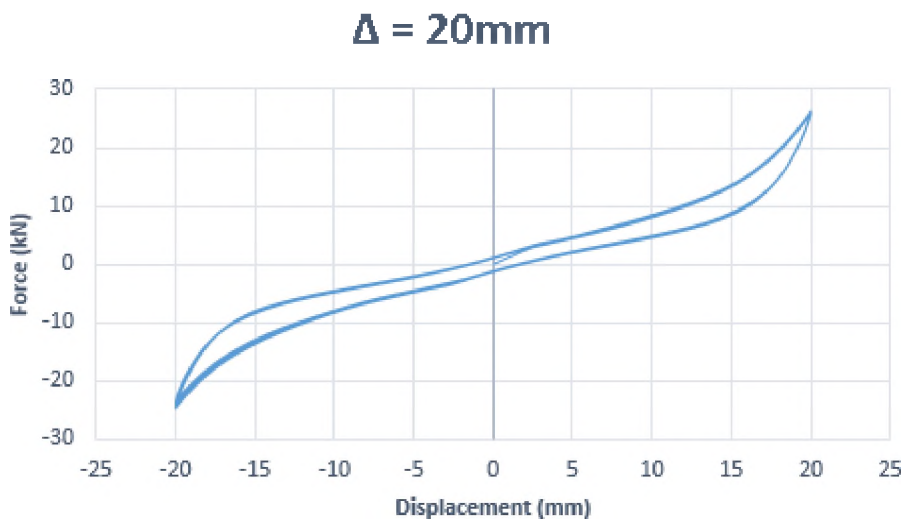

Figure 36 Force-displacement relationship of FE model subjected to fatigue cyclic loading (SMA material) at a displacement of 20 mm

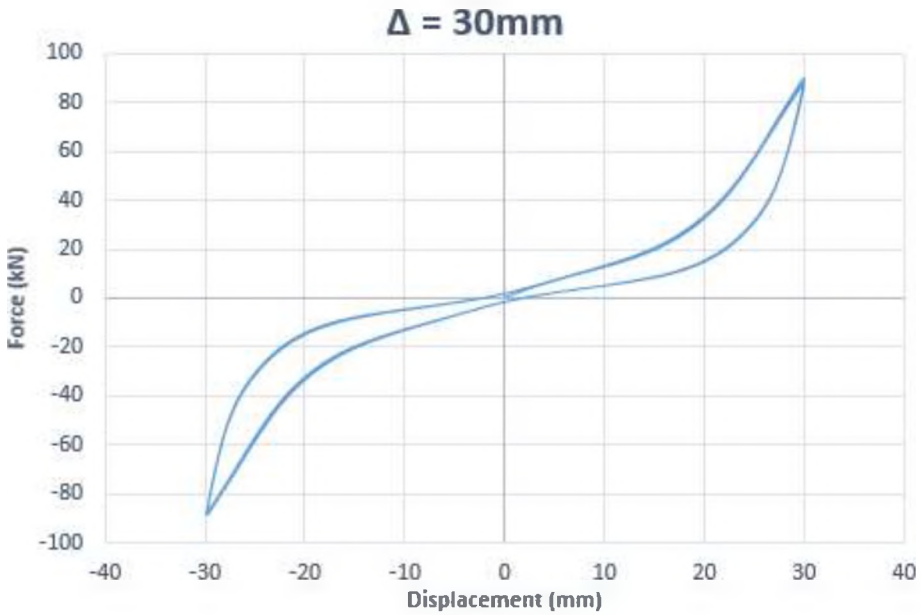

Figure 37: Force-displacement relationship of FE model subjected to fatigue cyclic loading (SMA material) at a displacement of 30 mm

4.3 Hysteretic behavior

4.3.1 Elastic-Plastic damper

Figure 33 displays the force-displacement relationship of specimens subjected to quasi-static cyclic loading. All specimens showed steady hysteresis loops and yielded in comparative small displacement. Before the dampers got into tensile strengthening phase, the hysteresis loops were comparable with flexural type metallic dampers. Specimens S1, S2 and S3 at 30th cycles had corresponding maximum forces as 51 kN, 55 kN and 62 kN respectively, which confirmed that the capacity of damper was independent on its height-thickness. Moreover, it can be seen that the tensile strengthening stage of damper established more completely than other steel plate dampers such as the "saw" type dissipaters (Demir and Husem, 2018), dual-pipe damper (DPD) (Maleki and Mahjoubi, 2013) and piston metallic damper (PMD) (Jarrah et al. 2019) in which the failure are predominantly caused by fracture of welding interface. The damper has a steadier flexural-tensile behavior. Since the theoretical derivation is established on the conjecture of superlative fixed boundaries, the theoretical values of the numerical studies as compared to Zhai et al. (2020) experimental test results are somehow dissimilar, i.e., the boundary conditions employed in the numerical analysis depicts what happens in the real cases, by making the end plates at the top and bottom fixed to the structure. In the experiment, such boundary conditions were not considered. A strength degradation was observed with the flag-shaped hysteresis loop after it reached its peak force. Figure 34 plots the Von Misses stress distribution of deformed models.

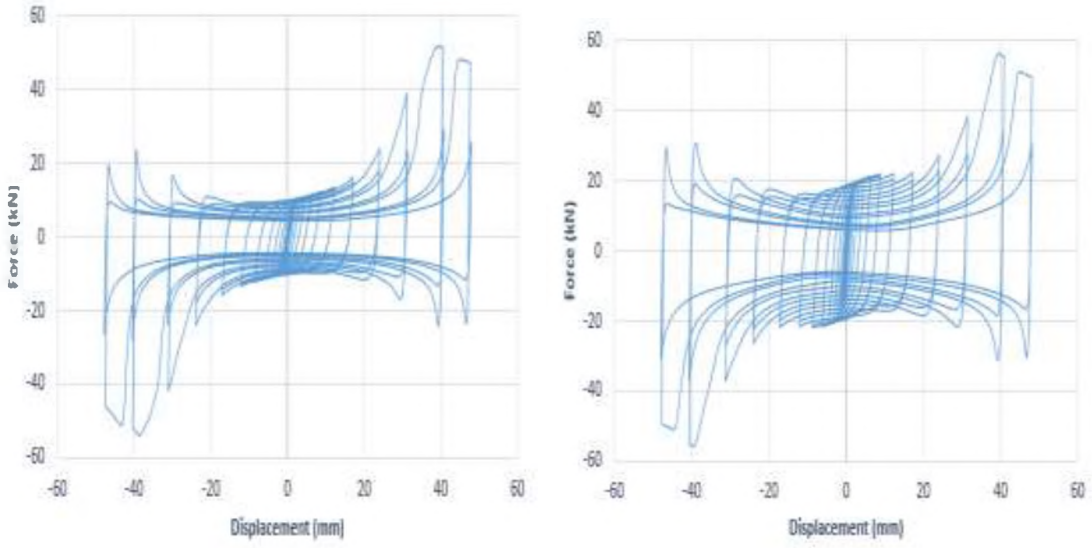

(a) S1 (b) S2

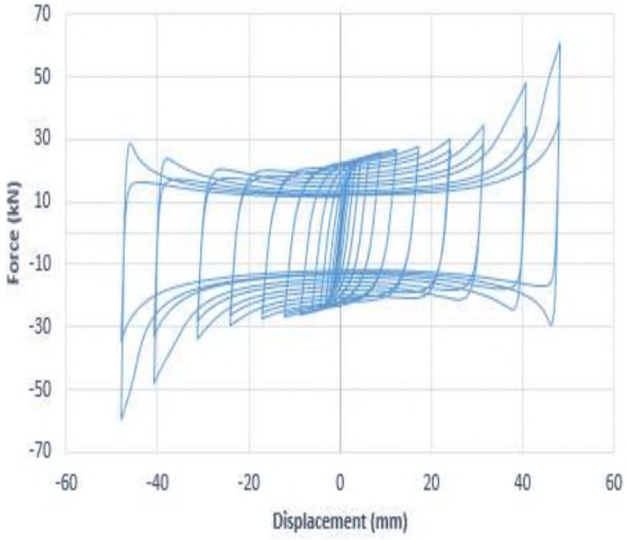

(c) S3

Figure 38: (a), (b) and (c) Force-displacement relationship of quasi-static tested dampers.

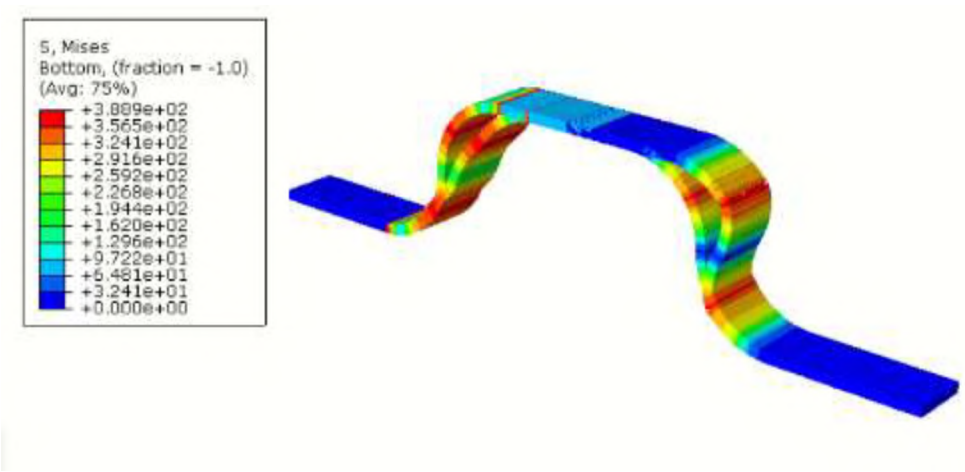

Figure 39: Von Mises stress distribution of deformed elastic-plastic FE models.

4.3.2 SMA damper

Figure 35 demonstrations the force–displacement hysteresis loop of the SMA dampers subjected to incremental loading amplitudes and with different damper thicknesses Steady and reasonable flag-shaped hysteresis loops without strength degradation in both positive and negative directions were observed. The SMA damper demonstrated satisfactory self-centering (SC) behavior without any residual deformation under cyclic loading. Wang and Zhu (2018) stated asymmetric stress–strain relationships of superelastic Nitinol under cyclic tension-compression loads. In the present simulation, the model parameters accounting for asymmetry in compression-shear and tension (ATC) were deactivated, hence, the SMA damper revealed nearly symmetrical hysteresis loops between the two loading directions. Moreover, this is also credited to the point that the SMA damper was subjected to tensile and compressive stresses concurrently in flexural behavior, thus showing a limited ATC effects. The works of Owusu-Danquah et al. (2015) demonstrated the ability of the utilized SMA model to capture the ATC effects in NiTi and NiTiHf actuators. It can be highlighted that related with figure 33 showing the cyclic response of the elastic-plastic damper coupon, figure 35 showed the stabilized hysteresis

loops of the SMA damper with insignificant strength degradation and residual deformation. It can be determined from the plots that, the SMA model S1, S2 and S3 have maximum force of 209 kN, 254 kN and 282 kN respectively. Figure 36 displays the Von Misses stress of deformed models.

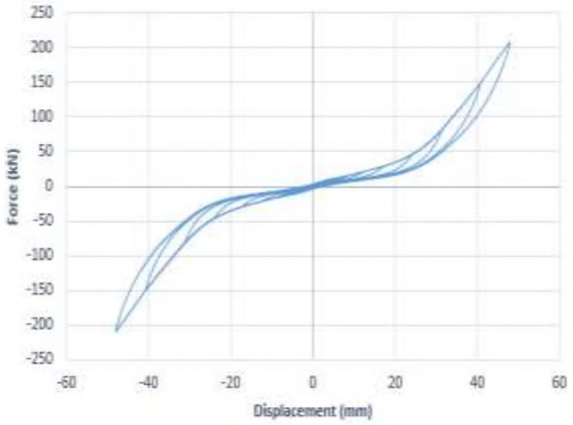

(a) S1

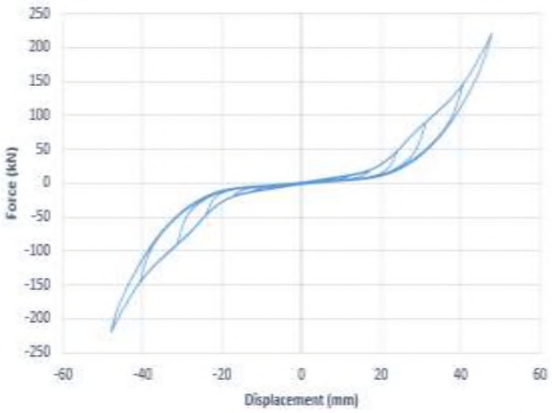

(b) S2

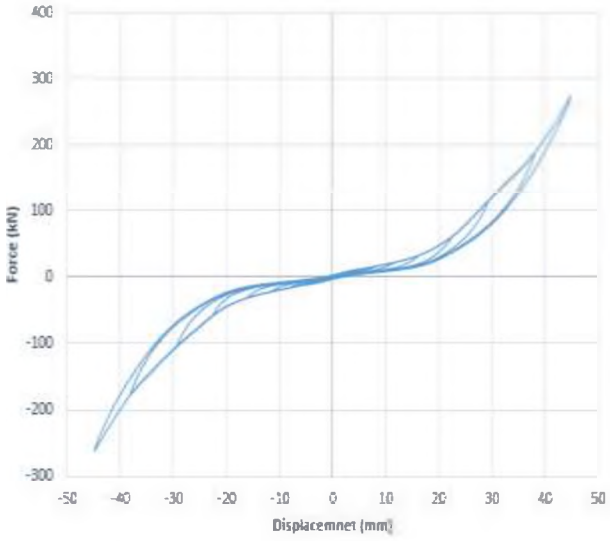

(c) S3

Figure 40:(a), (b) and (c) Force-displacement relationship of quasi-static tested SMA dampers.

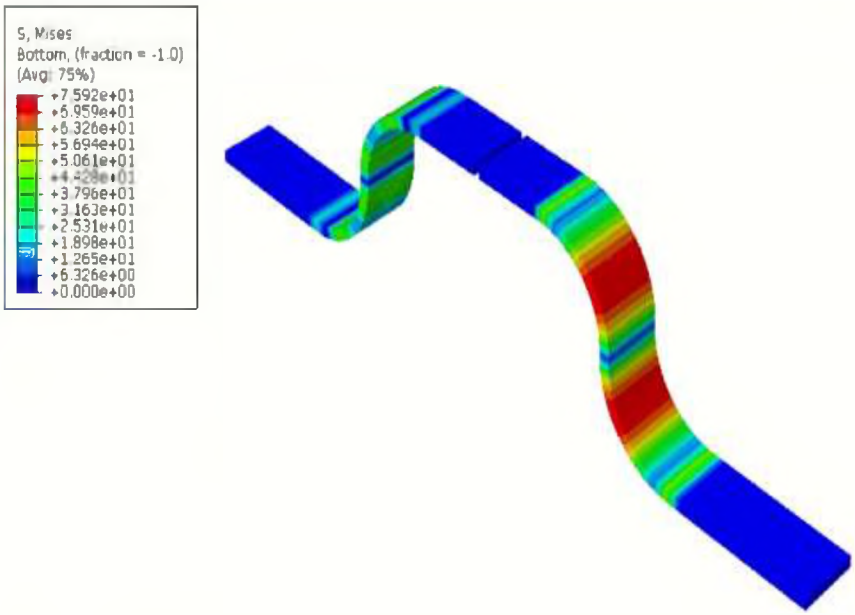

Figure 41: Von Mises stress distribution of deformed SMA FE models.

CHAPTER V

CONCLUSION AND FUTURE RESEARCH RECOMMENDATION

5.1 Conclusion

Large scale finite element simulations were conducted to evaluate the performance of a novel superelastic SMA S-shaped damper with self-centering capabilities. For comparison purposes, the experimental work executed by Zhai et al. (2020) for a steel material was used for initial part of the study. The primary objective was to investigate the effect of the material and geometry on the performance of the damper. An existing 3D SMA model was calibrated to capture the cyclic superelastic response of an additively manufactured NiTi material considered for the device. In the numerical simulations, several different types and numbers of elements were considered to assess their effect on the numerical results as well as computational time/cost. The seismic performance of the damper was evaluated under a series of monotonic and cyclic loading tests, i.e., a total of nineteen (19) cases.

The following conclusions highlight some of the important results gathered from the study:

1. The model predictions obtained from simulating the SMA stress-strain behavior under uniaxial loads, i.e., the material point response, was qualitatively similar to that resulting from the respective experiment.
2. The SMA S-shaped damper showed a steady hysteresis loop with excellent self-centering (SC) ability in all loading cases and cycles. Especially, under large displacements the damper demonstrated ideal self-centering (SC) behavior. This is primarily due to the type of SMA used. In particular, the displacement-force response characteristics of the structural device under non-homogeneous stress state was very much similar to stress-strain response of the simple homogeneous, uniaxial, experimental and model material-point tests responses.
3. In terms of the geometry, the height-thickness of the damper has significant influence on the material strength. The higher the thickness, the higher the peak force with a better strength.
4. The peak force of the hysteresis loop determined the material strength.
5. The percentage increase between the elastic plastic material and the SMA's for the S1, S2 and S3 were 76.6%, 78.35% and 78% respectively.

5.2 Future research

This study was limited to determining the seismic performance of a single type of SMA damper in terms of the strength, the peak force and the self-centering (SC) capabilities using numerical simulations. Therefore, further parametric studies can be conducted to study the energy dissipation capacity and strength-mass ratio of different types of SMA dampers with significant variations in materials and geometry. In particular, it will be interesting to consider novel high-temperature SMAs in the future studies as well

as confirm the present simulations with needed experiments for validation purposes. Also it is recommended that the study can be extended further in the following fields

i. Optimization of the shape of dampers

ii. Failure of Shape memory alloys (SMAs)

iii. Multiaxial deformation of SMA dampers.

REFERENCES

ABAQUS, 2013. Abaqus Analysis User's Manual. SIMULIA Inc., RI, USA.

ABAQUS Analysis User's Manual, Simulia, Dassault Systemes, Providence, RI, USA.

ABAQUS, v. 6.14 (2017). Computer software, Simulia, Dassault Systemes, Providence, RI, USA.

Aghlara, R., & Tahir, M. M. (2018). A passive metallic damper with replaceable steel bar components for earthquake protection of structures. Engineering structures, 159, 185-197.

Alam, M. S., Youssef, M. A., & Nehdi, M. (2007). Utilizing shape memory alloys to enhance the performance and safety of civil infrastructure: a review. Canadian Journal of Civil Engineering, 34 (9), 1075-1086.

Auricchio, F. (1995). Shape memory alloys: applications, micromechanics, macromodeling and numerical simulations. PhD Dissertation, Department of Civil and Environmental Engineering, The University of California at Berkeley.

Benavent-Climent, A. (2010). A brace-type seismic damper based on yielding the walls of hollow structural sections. Engineering Structures, 32(4), 1113-1122.

Bertram, A. (1983). Thermo-mechanical constitutive equations for the description of shape memory effects in alloys. Nuclear engineering and design, 74(2), 173-182.

Buehler, W. J., Gilfrich, J. V., and Wiley, R. C. (1963). Effect of low-temperature phase changes on the mechanical properties of alloys near composition TiNi. Journal of applied physics, 34(5), 1475-1477.

Buehler, W. J., and Wang, F.E. (1968). A summary of recent research on the nitinol alloys and their potential application in ocean engineering. Ocean Engineering, 1(1), 105-120

Chen, Y., Chen, C., Jiang, H., Liu, T., & Wan, Z. (2019). Study of an innovative graded yield metal damper. Journal of Constructional Steel Research, 160, 240-254.

Dal Lago, B., Biondini, F., & Toniolo, G. (2018). Experimental tests on multiple-slit devices for precast concrete panels. Engineering Structures, 167, 420-430.

Demir, S., and Husem, M. (2018). Saw type seismic energy dissipaters: development and cyclic loading test. Journal of Constructional Steel Research, 150, 264-276.

Deng, K., Pan, P., Li, W., & Xue, Y. (2015). Development of a buckling restrained shear panel damper. Journal of Constructional Steel Research, 106, 311-321.

Duerig, T. W., Melton, K. N., and Stöckel, D. W. C. M. (2013). Engineering aspects of shape memory alloys. Butterworth-Heinemann.

Elahinia, M. H., Hashemi, M., Tabesh, M., and Bhaduri, S. B. (2012). Manufacturing and processing of NiTi implants: A review. Progress in materials science, 57(5), 911-946.

Fugazza, D. (2003). Shape-memory alloy devices for earthquake engineering: mechanical properties, constitutive modeling and numerical simulations. MSc thesis, European School for Advanced Studies in Reduction of Seismic Risk, Pavia, Italy.

Funakubo, H., and Kennedy, J. B. (1987). Shape memory alloys. Gordon and Breach, xii+ 275, 15 x 22 cm, Illustrated.

Gagg, C. R., & Lewis, P. R. (2009). In-service fatigue failure of engineered products and structures–case study review. Engineering Failure Analysis, 16(6), 1775-1793.

Grabe, C., and Bruhns, O. T. (2009). Path dependence and multiaxial behavior of a polycrystalline NiTi alloy within the pseudoelastic and pseudoplastic temperature regimes. International Journal of Plasticity, 25(3), 513-545.

Guo, W., Ma, C., Yu, Y., Bu, D., & Zeng, C. (2020). Performance and optimum design of replaceable steel strips in an innovative metallic damper. Engineering Structures, 205, 110118.

Helm, D., and Haupt, P. (2002, July). Thermomechanical representation of the multiaxial behavior of shape memory alloys. In Smart Structures and Materials 2002: Active Materials: Behavior and Mechanics (Vol. 4699, pp. 343-354). International Society for Optics and Photonics.

Jarrah, M., Khezrzadeh, H., Mofid, M., and Jafari, K. (2019). Experimental and numerical evaluation of piston metallic damper (PMD). Journal of Constructional Steel Research, 154, 99-109.

Lagoudas, D. C. (Ed.). (2008). Shape memory alloys: modeling and engineering applications. Springer Science and Business Media.

Lee, C. H., Lho, S. H., Kim, D. H., Oh, J., & Ju, Y. K. (2016). Hourglass-shaped strip damper subjected to monotonic and cyclic loadings. Engineering Structures, 119, 122-134.

Li, Z., Shu, G., & Huang, Z. (2019). Development and cyclic testing of an innovative shear-bending combined metallic damper. Journal of Constructional Steel Research, 158, 28-40.

Lim, T. J., and McDowell, D. L. (1999). Mechanical behavior of an Ni-Ti shape memory alloy under axial-torsional proportional and nonproportional loading.

Mahrenholtz, C., Lin, P. C., Wu, A. C., Tsai, K. C., Hwang, S. J., Lin, R. Y., & Bhayusukma, M. Y. (2015). Retrofit of reinforced concrete frames with buckling-restrained braces. Earthquake Engineering & Structural Dynamics, 44(1), 59-78.

Maleki S, Mahjoubi S. (2013). Dual-pipe damper. J Constr Steel Res 2013;185:81–91.

McCormick, J., DesRoches, R., Fugazza, D., & Auricchio, F. (2007). Seismic Assessment of Concentrically Braced Steel Frames with Shape Memory Alloy Braces. Journal of Structural Engineering, 133 (6), 862-870.

McNANEY, J. M., Imbeni, V., Jung, Y., Papadopoulos, P., and Ritchie, R. O. (2003). An experimental study of the superelastic effect in a shape-memory Nitinol alloy under biaxial loading. Mechanics of materials, 35(10), 969-986.

Moghaddam, N. S., Saedi, S., Amerinatanzi, A., Hinojos, A., Ramazani, A., Kundin, J., ... & Elahinia, M. (2019). Achieving superelasticity in additively manufactured NiTi in compression without post-process heat treatment. Scientific reports, 9(1), 1-11.

Ölander, A. (1932). An electrochemical investigation of solid cadmium-gold alloys. Journal of the American Chemical Society, 54(10), 3819-3833.

Owusu-Danquah, J. S., Saleeb, A. F., Dhakal, B., & Padula, S. A. (2015). A comparative study of Ni 49.9 Ti 50.1 and Ni 50.3 Ti 29.7 Hf 20 tube actuators. Journal of Materials Engineering and Performance, 24(4), 1726-1740.

Ozbulut, O. E. (2007). Neuro-fuzzy model of superelastic shape memory alloys with application to seismic engineering. MSc thesis, Texas A&M University.

Penar, B. W. (2005). Recentering beam-column connections using shape memory alloys. MSc thesis, School of Civil and Environmental Engineering, Georgia Institute of Technology, Atlanta, GA.

Qu, B., Dai, C., Qiu, J., Hou, H., & Qiu, C. (2019). Testing of seismic dampers with replaceable U-shaped steel plates. Engineering Structures, 179, 625-639.

Rahid, G. (2013). Seismic vibration control of frame structure using shape memory alloys. MSc thesis, Department of Civil Engineering of Bangladesh University of Engineering and Technology, Dhaka.

Rogueda, C., Lexcellent, C., and Bocher, L. (1996). Experimental study of pseudoelastic behaviour of a Cu Zn AI polycrystalline shape memory alloy under tension-torsion proportional and non-proportional loading tests. Archives of Mechanics, 48(6), 1025-1047.

Sittner, P., Hara, Y., and Tokuda, M. (1995). Experimental study on the thermoelastic martensitic transformation in shape memory alloy polycrystal induced by combined external forces. Metallurgical and Materials Transactions A, 26(11), 2923-2935.

Sittner, P., Takakura, M., Hara, Y., and Tokuda, M. (1996). On transformation pathways of general stress controlled thermoelastic martensitic transformation in shape memory alloys. Le Journal de Physique IV, 6(C1), C1-357.

Tsai, K. C., Chen, H. W., Hong, C. P., & Su, Y. F. (1993). Design of steel triangular plate energy absorbers for seismic-resistant construction. Earthquake spectra, 9(3), 505-528.

Uchino, K., Otsuka, K., and Wayman, C. M. (1998). Shape memory materials.

Wang, B., and Zhu, S. (2018). Superelastic SMA U-shaped dampers with self-centering functions. Smart materials and structures, 27(5), 055003.

Whittaker, A. S., Bertero, V. V., José Luis Alonso G., & Thompson, C. (1989). Earthquake simulator testing of steel plate added damping and stiffness elements (Vol. 89, No. 2). Berkeley, CA, USA: Earthquake Engineering Research Center, University of California at Berkeley.

Xu, L. Y., Nie, X., & Fan, J. S. (2016). Cyclic behaviour of low-yield-point steel shear panel dampers. Engineering Structures, 126, 391-404.

Yang, T. Y., Li, T., Tobber, L., & Pan, X. (2020). Experimental and numerical study of honeycomb structural fuses. Engineering Structures, 204, 109814.

Zhai, Z., Guo, W., Yu, Z., He, C., and Zeng, Z. (2020). Experimental and numerical study of S-shaped steel plate damper for seismic resilient application. Engineering Structures, 221, 111006.

Zheng, J., Zhang, C., & Li, A. (2020). Experimental Investigation on the Mechanical Properties of Curved Metallic Plate Dampers. Applied Sciences, 10(1), 269.

Zibasokhan, H., Behnamfar, F., & Azhari, M. (2019). Experimental study of a new pure bending yielding dissipater. Bulletin of Earthquake Engineering, 17(7), 4389-4410.